

# INTERNAL AND EXTERNAL ALIGNMENT OF THE SHAPES AND ANGULAR MOMENTA OF $\Lambda$ CDM HALOS

JEREMY BAILIN<sup>1,2,3,4</sup> AND MATTHIAS STEINMETZ<sup>1,2,5,6</sup>

*Draft version November 15, 2018*

## ABSTRACT

We investigate how the shapes and angular momenta of galaxy and group mass dark matter halos in a  $\Lambda$ CDM  $N$ -body simulation are correlated internally, and how they are aligned with respect to the location and properties of surrounding halos. We explore these relationships down to halos of much lower mass ( $10^{11} h^{-1} M_{\odot}$ ) than previous studies. The halos are triaxial, with  $c/a$  ratios of  $0.6 \pm 0.1$  and a mean two-dimensional projected ellipticity of  $\langle e \rangle = 0.24$ . More massive halos are more flattened. The axis ratios rise out to  $0.6 r_{\text{vir}}$ , beyond which they drop. The principal axes, in particular the minor axes, are very well aligned within  $0.6 r_{\text{vir}}$ . High mass halos show particularly strong internal alignment. The angular momentum vectors are also reasonably well aligned except between the very outermost and very innermost regions of the halo. The angular momentum vectors tend to align with the minor axes, with a mean misalignment of  $\sim 25^{\circ}$ , and lie perpendicular to the major and intermediate axes. The properties of a halo at  $0.4 r_{\text{vir}}$  are quite characteristic of the properties at most other radii within the halo. There is a very strong tendency for the minor axes of halos to lie perpendicular to large scale filaments, and a much weaker tendency for the major axes to lie along the filaments. This alignment extends to much larger separations for group and cluster mass halos than for galaxy mass halos. As a consequence, the intrinsic alignments of galaxies are likely weaker than previous predictions, which were based on the shapes of cluster mass halos. The angular momenta of the highest concentration halos tend to point toward other halos. The angular momenta of galaxy mass halos point parallel to filaments, while those of group and cluster mass halos show a very strong tendency to point perpendicular to the filaments. This suggests that group and cluster mass halos acquire most of their angular momentum from major mergers along filaments, while the accretion history of mass and angular momentum onto galaxy mass halos has been smoother.

*Subject headings:* galaxies: formation — galaxies: halos — galaxies: structure — dark matter — galaxies: clusters: general — methods: N-body simulations

## 1. INTRODUCTION

The three-dimensional structure of the dark matter halos that host galaxies, groups, and clusters is an important aspect of their nature that can provide insight into their formation and affect the luminous structures within. The orientation of the halo shapes and angular momenta, both internally and with respect to surrounding halos, provide important constraints on other studies of galaxy formation and evolution.

Halos formed in cosmological simulations are generally not spherical, but have an ellipsoidal shape. There have been several studies of the shapes of halos in low resolution  $N$ -body simulations based on the standard cold dark matter (CDM) paradigm (Frenk et al. 1988; Dubinski & Carlberg 1991; Warren et al. 1992 (hereafter W92); Cole & Lacey 1996). These studies have found that halos are usually triaxial, with a preference for prolate figures at small radii and more oblate figures at large radii, and have minor-to-major axis ratios ranging from 0.3 to almost unity. Dubinski & Carlberg (1991), in sim-

ulations of the formation of isolated galaxies where the effects of the external tidal field were prescriptively superimposed, found that the projected two-dimensional ellipticities peak around  $e = 0.5$ , where

$$e \equiv 1 - q, \quad (1)$$

for a projected axis ratio of  $q$ . W92 found that while this holds in the inner regions, the location of the peak falls to  $e = 0.25$  beyond 50 kpc. The behaviour of the axis ratios with radius is controversial; Dubinski & Carlberg (1991) and W92 find that the axis ratios increase (become more spherical) with radius, while Frenk et al. (1988) and Cole & Lacey (1996) find that they decrease with radius. W92 have also studied the internal alignment of the ellipsoid principal axes. They found that both the major and minor axes of halos are extremely well aligned out to 40 kpc.

More recently, several authors have performed large high resolution simulations using the currently-favoured  $\Lambda$ CDM cosmology (Bullock 2002; Jing & Suto 2002 (hereafter JS02); Kasun & Evrard 2004 (hereafter KE04); Hopkins et al. 2005 (hereafter HBB05)). Bullock (2002) finds that the  $c/a$  axis ratios are a strong function of halo mass, and range from 0.55 at  $10^{14} h^{-1} M_{\odot}$  to 0.7 around  $10^{12} h^{-1} M_{\odot}$ , with a distribution that is peaked but has a large tail to small axis ratios. He also finds that the inner  $30 h^{-1}$  kpc of halos are more spherical than the outer regions, i.e. the axis ratios decrease with radius. On the other hand, JS02 find  $c/a$  axis ratios that increase

<sup>1</sup> Steward Observatory, University of Arizona, 933 N Cherry Ave, Tucson, AZ 85721 USA

<sup>2</sup> Astrophysikalisches Institut Potsdam, An der Sternwarte 16, D-14482 Potsdam, Germany

<sup>3</sup> Swinburne University of Technology, Mail H39, PO Box 218, Hawthorn, VIC 3121 Australia

<sup>4</sup> jbailin@astro.swin.edu.au

<sup>5</sup> msteinmetz@aip.de

<sup>6</sup> David and Lucile Packard Fellow

with radius, decrease slightly with mass, and are well fit by a Gaussian centred at  $c/a = 0.55$  with a width of 0.11. They find that the major axes of halos are relatively well aligned — typically  $\cos \theta_{11} \sim 0.8$ , where  $\theta_{11}$  is the angle between the major axis at small or large radius compared to that at an intermediate radius. The alignment of the middle axes is somewhat poorer, but JS02 argue that this is due to the inclusion of nearly prolate halos whose axes are degenerate and therefore not well determined. KE04 find more spherical shapes in their very large sample of high mass halos ( $M > 3 \times 10^{14} h^{-1} M_{\odot}$ ), possibly due to the spherical outer boundary they impose, with  $c/a \approx 0.65$ . HBB05 measure the intermediate-to-major axis ratio  $b/a$  of cluster mass halos and find a mean of 0.67, with a mass dependence similar to that found by Bullock (2002), and axis ratios that decrease with radius.

The shapes of dark matter halos can have important observational consequences (for a good review, see Sackett 1999). On galactic scales, they can affect the coherence of tidal streams. Some authors have claimed that the thinness of the tidal stream associated with the Sagittarius dwarf spheroidal indicates that the halo of the Milky Way is nearly spherical, with  $c/a \gtrsim 0.8$  (Ibata et al. 2001; Johnston et al. 2005; Martínez-Delgado et al. 2004). However, more recent studies suggest that the material that makes up the stream was stripped from the satellite too recently to have had time to undergo differential precession, which severely weakens the constraints on the halo shape (Helmi 2004a,b). Helmi (2004b) even claims that the stream is best fit assuming a prolate halo elongated perpendicular to the disk with  $c/a \approx 0.6$ . Law, Johnston, & Majewski (2005) also find that the velocities of stars in the leading stream can only be fit with a prolate halo, but that the precession of the leading stream with respect to the trailing stream can only be fit with an oblate halo. These contradictory results suggest that evolution of the satellite orbit or other effects of a live Milky Way potential (as opposed to the static potential that has been used in all of these studies) are important for determining the shape of the Milky Way halo using the Sgr stream. Other measures of the Milky Way ellipticity using the flaring of the gas disk at large radius or the anisotropy of stellar velocities suggest that the halo is oblate with a flattening of  $c/a \sim 0.8$  (Olling & Merrifield 2000). The shapes of the halos of external galaxies can be measured using the flaring of the gas layer (Olling & Merrifield 2000), the projected shape of X-ray gas (Buote et al. 2002), or the kinematics of polar ring galaxies (Sackett et al. 1994). These methods suggest that galaxy halos have a wide range of flattenings from  $c/a \sim 0.3 - 0.8$ . Assuming that the shape of the stellar halo traces that of the dark matter halo, the stacked images of edge-on disk galaxies in the Sloan Digital Sky Survey are consistent with a mean  $c/a = 0.6$  (Zibetti et al. 2004). A new method for measuring the shapes of external galaxy halos is weak gravitational lensing. By measuring the azimuthal variation of the shear with respect to the position angle of the visible lens galaxy (Natarajan & Refregier 2000), Hoekstra et al. (2004) detected an average projected halo ellipticity of  $\langle e \rangle = 0.33$  for halos with an average mass of  $8 \times 10^{11} h^{-1} M_{\odot}$ . This detection also implies that the orientation of the visible and dark mass in galaxies must be

similar. On group and cluster scales, X-ray observations and the Sunyaev-Zeldovich effect (Sunyaev & Zeldovich 1980) can be directly used as a probe of halo ellipticities (Lee & Suto 2003, 2004).

The orientation of the angular momentum in halos has also been studied in cosmological numerical simulations. Early low-resolution studies (Barnes & Efstathiou 1987; Frenk et al. 1988; Cole & Lacey 1996) gave conflicting results due to the difficulty of measuring the direction of the angular momentum with few particles. Other CDM studies (Dubinski 1992; W92) have found that the direction of the angular momentum at different radii is usually the same, but that the distribution of alignments has a tail that stretches all the way to anti-alignment. This result is verified by recent high-resolution  $\Lambda$ CDM simulations (Bullock et al. 2001a). CDM studies have also found that the angular momentum is most often aligned with the minor axis and perpendicular to the major axis, although there is some scatter (Dubinski 1992; W92). This result has not yet been thoroughly tested in high-resolution  $\Lambda$ CDM simulations.

Internal misalignment of the angular momentum can have a number of observational consequences. It may cause galactic warps (Ostriker & Binney 1989; Debattista & Sellwood 1999; López-Corredoira et al. 2002; Bailin 2004), or manifest itself in anisotropic distributions of the orbits of satellite galaxies (Holmberg 1974; Zaritsky et al. 1997; Aubert et al. 2004; Knebe et al. 2004).

Going beyond individual halos, the shapes and angular momenta of nearby halos can be correlated due to initial conditions or dynamical evolution. This subject has attracted increased interest recently due to the emergence of weak gravitational lensing as a method to measure the projected mass density in front of background galaxies. Intrinsic correlations between the projected shapes of luminous galaxies act as spurious background signals in weak lensing, so predicting their magnitude is important. At a more fundamental level, the degree of correlation between structures can be tested against models, and can inform our understanding of the origin of halo shapes and angular momenta.

Measurements of halo alignments and correlations come from two sources: cluster orientations and large galaxy surveys. The study of the alignment of cluster orientations was pioneered by Binggeli (1982), who used the locations of the constituent galaxies to determine that the major axes of clusters separated by less than  $15 h^{-1}$  Mpc tend to point toward each other. While some authors have not found any such alignment (e.g. Struble & Peebles 1985), larger samples of both galaxies and clusters, along with improved error estimates, have confirmed this result (e.g. Flin 1987; Rhee & Katgert 1987; Plionis 1994). Similar results are seen when using the major axis of the brightest cluster galaxy as a measurement of the cluster orientation (Lambas et al. 1990). Enhancements in galaxy counts along the major axis of brightest cluster galaxies out to  $15 h^{-1}$  Mpc have also been detected (Argyres et al. 1986; Lambas et al. 1988; Muriel & Lambas 1989). The cluster potential is better probed by X-ray emitting gas (Sarazin 1986; Lee & Suto 2003, 2004). While early studies using X-ray contours found no alignment of clusters with the large scale structure (Ulmer et al. 1989), more and better data

have confirmed that the orientation of both the substructure and the main cluster potential tends to point toward neighbouring clusters (West et al. 1995; Chambers et al. 2002).

While the principal axes of clusters can be determined from optical or X-ray photometry, the angular momentum direction is very difficult to determine. In disk galaxies, on the other hand, the angular momentum direction of the baryons, presumed to be perpendicular to the orientation of the disk, can be measured much more easily than the shape of the dark matter halo. Although there may be some misalignment between the angular momentum of the baryons and dark matter (van den Bosch et al. 2002; Sharma & Steinmetz 2004), spiral galaxies still provide the best targets for detecting angular momentum alignments and correlations. Studies with small samples of spiral galaxies (less than a few hundred) have generally found no correlation between the orientation of the angular momentum and the large scale structure (Černe & Peterson 1990; Han et al. 1995; Cabanela & Dickey 1999; see however Navarro, Abadi, & Steinmetz 2004). With a sample of 618 lenticular and disk galaxies in the local supercluster, Kashikawa & Okamura (1992) found that while the full sample was consistent with an isotropic distribution of angular momenta, those galaxies within  $2 h^{-1}$  Mpc of the supergalactic plane tend to have spin vectors pointing in the plane, while those above or below the plane tend to have spin vectors that point toward or away from the plane. Navarro et al. (2004) also find a clear excess of galaxies whose angular momenta lie in the supergalactic plane. Larger samples of galaxies provide further evidence of alignments between spin and the large scale structure: Pen, Lee, & Seljak (2000) have found that the spin directions of the 12,122 spiral galaxies in the Tully catalog are positively correlated at separations less than  $3 h^{-1}$  Mpc, while Brown et al. (2002) have measured intrinsic correlations between galaxy orientations at a range of angular separations in the  $2 \times 10^6$  galaxies of the SuperCOSMOS survey.

Linear tidal torque theory (Doroshkevich 1970; White 1984) can be used to predict the directions of the angular momentum vectors and their correlations with the surrounding structure (Pen et al. 2000; Lee & Pen 2000, 2001; Crittenden et al. 2001; Porciani et al. 2002a,b). These studies have found that the angular momenta of halos tend to lie perpendicular to the large scale structure, and that the correlation of the halo spin vectors with each other exists but is very weak. While tidal torque theory performs reasonable well at predicting the evolution of the magnitude of the angular momentum (Sugerman et al. 2000), Porciani et al. (2002a) have tested the predictions of spin directions against  $N$ -body simulations, and found that the spin axes of  $N$ -body halos show significant misalignment compared to the tidal torque predictions, with a mean misalignment of  $\sim 50^\circ$  at  $z = 0$ . Therefore,  $N$ -body simulations that take the full non-linear dynamics into account are necessary.

Some early numerical work at predicting the intrinsic alignments using simulations with power law or CDM power spectra found that the major axes of cluster mass halos tend to point toward other nearby clusters over scales of  $\sim 15 h^{-1}$  Mpc, and that there is a very weak tendency for the major axes to be correlated with each other

over the same range of separations (Barnes & Efstathiou 1987; West et al. 1991; van Haarlem & van de Weygaert 1993; Splinter et al. 1997). More recent high resolution  $N$ -body simulations in a  $\Lambda$ CDM cosmology have been studied to search for alignments of the major axes (Onuora & Thomas 2000; KE04; HBB05), the angular momentum vectors (Hatton & Ninin 2001), or both (Faltenbacher et al. 2002; hereafter F02). These studies have found a strong tendency for the major axes of cluster mass halos to point toward other clusters out to several tens (or even hundreds) of Mpc and to correlate with each other out to  $20 h^{-1}$  Mpc. The situation for the angular momentum is murkier. Hatton & Ninin (2001) have found that the angular momenta of halos tend to lie parallel to the large scale structure, while F02 have found that they lie perpendicular to the large scale structure, in agreement with the prediction from the linear theory (Lee & Pen 2001). Correlations of halo angular momentum vectors with each other appear weak at best. Two groups have searched specifically for correlations between the ellipticities of  $z \approx 1$  galaxies in the Virgo Consortium  $\Lambda$ CDM model (Jenkins et al. 1998) in order to predict the effect on weak lensing signals. Croft & Metzler (2000) assumed that the shapes of the galaxies were identical to the shapes of the dark matter halos, while Heavens et al. (2000) (hereafter HRH00) made separate predictions about ellipticals, which were assumed to share the shape of their dark matter halos, and spirals, which were assumed to lie orthogonal to the halo angular momentum. In both cases, the correlations are small, but detectable.

In this paper, we present an extensive study of the shapes of galaxy and group-mass halos in a large high resolution  $\Lambda$ CDM  $N$ -body simulation. We study the internal alignments of all of the principal axes and the angular momentum. We also study the alignment of all of these quantities with the large scale structure, and how they are correlated in halos of different separations. This work improves upon earlier studies of the internal structure of halos by using large high resolution simulations in a currently-favoured  $\Lambda$ CDM cosmology, by studying both the alignment of the angular momentum and the shape, and by using a method that allows us to quantify our errors and therefore feel confident about the source of any measured misalignments. Previous external alignment studies have all been restricted to massive clusters; we improve upon this significantly by reaching down to galaxy mass halos, by studying the mass dependence of the correlations, by studying the alignments of both the principal axes and the angular momenta, and by including the oft-neglected intermediate and minor axes. The structure of the paper is as follows. In § 2 we present the details of the simulation and describe the method used to measure the principal axes and angular momentum vectors of the halos. § 3 presents the overall shapes of the halos and how they change with radius. We discuss the internal alignment of the principal axes and angular momenta in § 4, while we explore the alignment of these quantities with external halos in § 5. We discuss what these results imply for the origin of halo shapes, angular momentum, and warped galaxies in § 6, and summarize the results in § 7.

### 2.1. The simulation

The simulation used here is the same as the one used in Bailin & Steinmetz (2004). It consists of  $512^3$   $N$ -body particles in a periodic box of length  $50 h^{-1}$  Mpc, in a low density flat universe ( $\Omega = 0.3$ ,  $\Omega_\Lambda = 0.7$ ,  $h = 0.7$ ,  $\sigma_8 = 0.9$ ). The particle mass is  $7.757 \times 10^7 h^{-1} M_\odot$ , and the force softening length is  $5 h^{-1}$  kpc. Halos were found using the standard friends-of-friends (FOF) algorithm with a linking length of 0.2 times the mean inter-particle separation.

In order to accurately measure the direction of the principal axes, a sufficiently large number of particles per halo are required. The direction of an axis can generally be determined to within an angle of

$$\theta_{\text{err}} = \frac{1}{2\sqrt{N}} \frac{\sqrt{r}}{1-r} \text{ radians}, \quad (2)$$

where  $N$  is the number of particles used and  $r$  is the relevant axis ratio:  $b/a$  for the major axis,  $c/b$  for the minor axis, and  $\max(b/a, c/b)$  for the intermediate axis (see Bailin & Steinmetz 2004). For the purposes of measuring internal alignments, we would like the angular errors to be less than  $10^\circ$ . This requires on the order of 200 particles. Since each halo is split up into 6 radial shells, and this accuracy is required in each shell, each halo should have over 1200 particles. For convenience, we adopt a cutoff of  $10^{11} h^{-1} M_\odot$  for the mass of the halo, or 1289 particles.

There are 3869 halos in the sample with masses extending from  $10^{11} h^{-1} M_\odot$  to  $2.8 \times 10^{14} h^{-1} M_\odot$ . 451 of the halos have masses in the range  $10^{12} - 10^{13} h^{-1} M_\odot$ , while 62 of the halos have masses greater than  $10^{13} h^{-1} M_\odot$ .

### 2.2. Measuring the axes

A standard technique to measure halo triaxiality in simulations is to use an iterative approach, where the particles are initially chosen to lie in a sphere or spherical shell, an ellipsoid is fit to these particles, and particles are chosen for the next iteration based on the new ellipsoid (e.g. W92). While this works for simulations that have sufficiently low resolution that overmerging erases substructure, we find in agreement with JS02 that in high resolution simulations, the presence of substructure prevents this technique from converging for a large fraction of halos.

JS02 have adopted a novel approach aimed at directly measuring isodensity contours. They assign SPH-like densities to halo particles, and then measure the principal axes and axis ratios of particles with densities near the nominal density of the isodensity contour. Due to the presence of substructure, this procedure often picks out disconnected shells in addition to the particles that define the isodensity contour of the smooth distribution. JS02 use the FOF algorithm to select the largest structure that fulfils the density criterion and therefore eliminate the substructure.

While this algorithm works well for very high-resolution halos, such as those JS02 use to demonstrate the technique (all of which contain  $N > 6 \times 10^5$  (Jing & Suto 2000)), we encountered difficulties using it on more moderate resolution halos. In particular, we find that it is not possible to find an optimal FOF linking length for eliminating substructure; if the linking length

is too large, many ‘‘contours’’ contain obvious disconnected substructures, while reducing the linking length sufficiently to eliminate this problem reduces it to the point where in many halos, the single ellipsoid corresponding to the smooth distribution is broken up by the algorithm into several disconnected pieces. JS02’s algorithm also uses a relatively small number of particles to determine the shape. The error in the determination of the direction of the principal axes of a particle distribution goes as  $N^{-1/2}$  (see eq. [2]). Measuring the internal alignment of a halo requires small well-understood errors, and therefore as many particles as possible.

We take the following approach, similar to that taken by Frenk et al. (1988). The center of mass is calculated iteratively in spheres centred on the center of mass of the sphere in the previous iteration, starting with a sphere containing all of the particles. The radius of each successive sphere is reduced by 90%, and the procedure is iterated 25 times, by which point it has converged. The particles of each halo are transformed into this center of mass frame, and the velocities are transformed into the center of velocity frame. Each halo is then divided up into six concentric spherical shells with outer radii  $R$  of 1.0, 0.6, 0.4, 0.25, 0.12, and 0.06 times the virial radius  $r_{\text{vir}}$ . These radii are chosen to allow easy comparison to the isodensity contours of JS02. The outer radius of each shell also forms the inner radius of the next larger shell, except for the innermost ‘‘shell’’, which is actually a sphere extending to the halo center. One would like to use the inertia tensor to measure the principal axes of the mass distribution. However, the inertia tensor can be dominated by substructure in the outer part of the shell. Therefore, we weight particles by  $1/r^2$  so that each mass unit contributes equally regardless of radius (Gerhard 1983). Within each shell, we calculate this reduced moment of inertia tensor

$$\tilde{I}_{ij} = \sum_k \frac{r_{k,i} r_{k,j}}{r_k^2}, \quad (3)$$

which we then diagonalize. The axis ratios  $a$ ,  $b$ , and  $c$  are the square roots of the eigenvalues ( $a \geq b \geq c$ ), and the eigenvectors give the directions of the principal axes. There are no particles in common between radial shells, so the measurements of the axes at different radii are completely independent. We also calculate the angular momentum of the particles in each shell.

To calculate the error in the axis and angular momentum determinations, we perform a bootstrap analysis of the particles in each radial shell (Heyl et al. 1994). If the shell contains  $N$  particles, we resample the shell by randomly selecting  $N$  particles from that set allowing for duplication and determine the axes and angular momentum from this bootstrap set. We do this 100 times for each radial shell. The dispersions of these estimates of the axis ratios, directions of the axes, magnitude of the angular momentum, and direction of the angular momentum around the measured values are taken formally as the ‘‘ $1\sigma$ ’’ error of each of these quantities.

Using spherical shells, rather than the ellipsoids defined by the isodensity contours as in JS02, does not affect the orientation of the principal axes. It does, however, bias the derived axis ratios toward spherical. To calibrate the magnitude of this bias, we have constructed prolate Poisson-sampled NFW

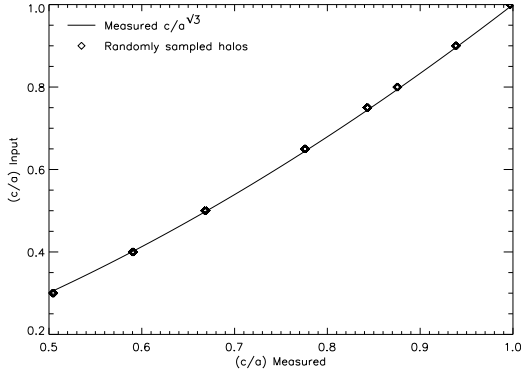


FIG. 1.— Measured versus input  $c/a$  axis ratio of randomly-sampled NFW and singular isothermal halos. At each input axis ratio, there are 12 independent points, representing the results for each of six radial bins and two different density profiles, but they are virtually indistinguishable. The solid line is the empirical fit of equation (4).

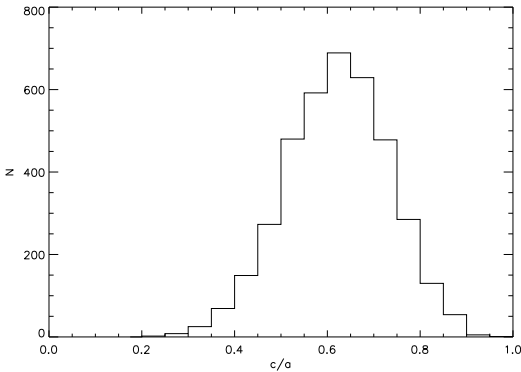


FIG. 2.— Histogram of the minor-to-major  $c/a$  axis ratio for each halo in the simulation, as measured in the  $R = 0.4 r_{\text{vir}}$  shell.

(Navarro, Frenk, & White 1996) and singular isothermal halos with  $10^5$  particles each that have known  $c/a$  axis ratios ranging from 0.3 – 1. The NFW halos had concentration parameters  $c_{\text{vir}} = 10$ . In Figure 1 we plot the input  $c/a$  axis ratio for each combination of radial bin and density distribution as a function of the  $c/a$  ratio measured for the halos constructed using the method described above. The points for different radii and density distributions are virtually indistinguishable; the only important parameter is the input axis ratio. The solid line is an empirical fit to these points:

$$(c/a)_{\text{true}} = (c/a)_{\text{measured}}^{\sqrt{3}}. \quad (4)$$

The relationship for  $b/a$  is identical. The corrected axis ratios  $(b/a)_{\text{true}}$  and  $(c/a)_{\text{true}}$  are used throughout the remainder of this paper.

### 3. SHAPES

Dark matter halos are well approximated by ellipsoids (JS02) and are well described by the intermediate-to-major and minor-to-major axis ratios  $b/a$  and  $c/a$ . Figure 2 is a histogram of the  $c/a$  axis ratios as measured in the  $R = 0.4 r_{\text{vir}}$  shell for all of the halos in our sample. Unlike JS02, we find that they are not quite Gaussian, but rather have a tail toward very flattened halos as seen

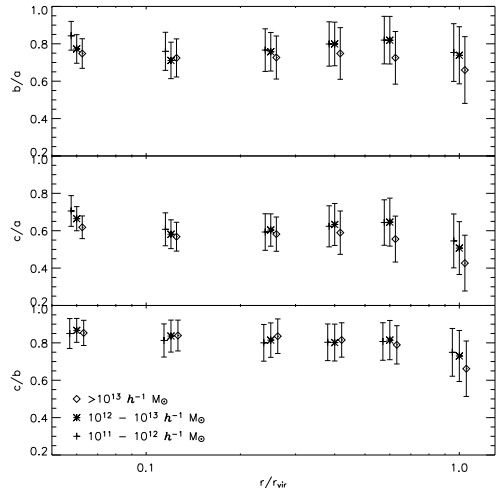


FIG. 3.— Median of the  $b/a$  (top),  $c/a$  (middle), and  $c/b$  (bottom) axis ratios for each radial shell. Crosses, asterisks, and diamonds represent the mass ranges  $10^{11} - 10^{12} h^{-1} M_{\odot}$ ,  $10^{12} - 10^{13} h^{-1} M_{\odot}$ , and  $10^{13} - 3 \times 10^{14} h^{-1} M_{\odot}$  respectively. Error bars represent the  $1\sigma$  width of the distribution. The error in the median is typically 0.002 for the crosses, 0.005 for the asterisks, and 0.01 for the diamonds — smaller than the sizes of the symbols. Crosses and diamonds are offset in radius for clarity.

by KE04, although the tail is not as extreme as that seen by Bullock (2002). The distribution of  $b/a$  and  $c/a$  values measured at other radii have a similar shape. The lack of very flattened halos in JS02 may be a result of their exclusion of halos deemed to be interacting. The axis ratios we find are intermediate between the quite flattened halos found by JS02 and the more spherical halos found by KE04.

Early studies suggested that the coldness of the Sgr stream indicates that the dark matter halo of the Milky Way has  $c/a \gtrsim 0.8$  (Ibata et al. 2001; Johnston et al. 2005; Martínez-Delgado et al. 2004). Only 5% of the halos shown in Figure 2 have axis ratios so large. While this is not negligible, it is uncomfortably small, and forces us into the anti-Copernican situation of living in an exceptional galaxy. However, new models of the Sgr stream that are more careful about matching observations of the body of the dwarf find that the stars that constitute the stream were stripped from the body of the satellite too recently to have had time to undergo differential precession, thereby severely weakening the constraints on the halo ellipticity (Helmi 2004a,b); current models are unable to simultaneously fit the velocities of stars in the leading stream and the orbital planes of the leading and trailing streams (Law et al. 2005). It should also be noted that our simulations do not take into account the effects of baryonic physics. There is some evidence that baryon cooling leads to more spherical halos (Dubinski 1994; Kazantzidis et al. 2004). Therefore systems in which most of the baryons have cooled, such as disk galaxies like the Milky Way, may have dark matter shapes that are more spherical than those presented here. Observations of external galaxies using a variety of methods find halo flattenings that range from 0.3 to 0.8, in agreement with our results (Sackett 1999).

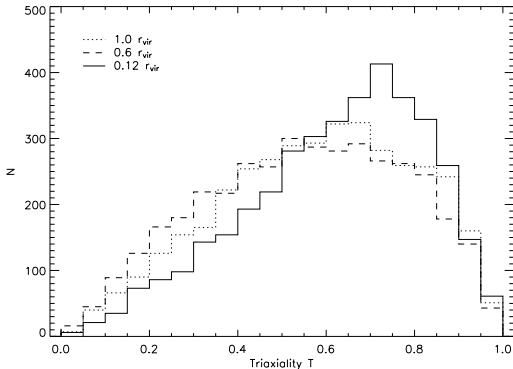


FIG. 4.— Histogram of the triaxiality  $T$  of all halos. The solid, dashed, and dotted histograms represent the halos measured at  $0.12$ ,  $0.6$ , and  $1.0$   $r_{\text{vir}}$  respectively.

The radial dependence of the axis ratios is shown in Figure 3. There are three distinct regions of the halo. Over most of the halo, the axis ratios increase with radius (i.e. the halos become more spherical). Near the virial radius, infalling unvirialized structure causes the axis ratios to drop. In the central 6% of the virial radius, the axis ratios rise. However, this is probably an artifact of the numerical softening (Bailin & Steinmetz 2004). Further evidence that this is a numerical effect comes from examining the location of this increase in sphericity for halos of different mass. The increase occurs at a larger fraction of the virial radius for low mass halos, i.e. at a similar physical radius. This complicated and non-monotonic radial dependence may explain the discrepancy between studies that have found that flattening increases with radius (Frenk et al. 1988; Cole & Lacey 1996; Bullock 2002) and those that have found that it decreases with radius (Dubinski & Carlberg 1991; W92; JS02; HBB05). The mass dependence of the axis ratios is shown by the different symbols in Figure 3. The highest mass halos have smaller axis ratios at all radii than the smaller halos (W92; Bullock 2002; JS02; KE04). Our halos extend down to masses an order of magnitude smaller than any other study; the difference between the most massive halos (the diamonds) and the galaxy mass halos is more pronounced than the difference between different masses of galaxy halos. The high mass halos show particularly strong flattening near the virial radius.

As seen in Figure 3, the  $c/b$  ratio falls steadily with radius, indicating a transition from prolate figures in the center to oblate figures at large radii (Dubinski & Carlberg 1991; W92). Triaxiality can be quantified by the parameter  $T$ :

$$T = \frac{a^2 - b^2}{a^2 - c^2} \quad (5)$$

(Franx et al. 1991). Purely prolate halos have  $T = 1$  while purely oblate halos have  $T = 0$ . We have measured  $T$  at three radii:  $R = 1.0$   $r_{\text{vir}}$ , where infalling material results in substantial flattening,  $R = 0.6$   $r_{\text{vir}}$ , where the halos are at their least flattened, and  $R = 0.12$   $r_{\text{vir}}$ , where the interior of the halos are at their most flattened. Histograms of  $T$  at these radii are shown in Figure 4. The interior regions of halos clearly tend to be prolate (solid histogram). As the flattening decreases at larger

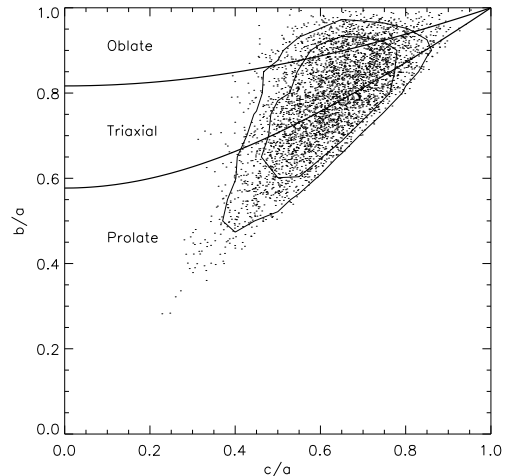


FIG. 5.— Intermediate axis ratio  $b/a$  as a function of minor axis ratio  $c/a$  for all of the halos, measured at  $R = 0.4$   $r_{\text{vir}}$ . The inner and outer contours enclose 68% and 90% of the halos respectively. The thick lines have constant values of the triaxiality parameter  $T$ . The separations between the prolate, triaxial, and oblate populations occur at  $T = 1/3$  and  $2/3$ .

radii, many of the halos become more oblate (dashed histogram), although still more are prolate than oblate. Near the virial radius, there is a small shift back toward prolate shapes (dotted histogram). Figure 5 shows the full relationship between  $b/a$  and  $c/a$  for all of the halos in our sample, measured at  $R = 0.4$   $r_{\text{vir}}$ , where the values are most typical for the halo as a whole. The preponderance of prolate and triaxial halos over oblate halos is clearly seen.

HBB05 examined the evolution of ellipticity of cluster mass halos at a wide range of redshifts in a  $\Lambda$ CDM simulation, and found that halos of a given mass have higher ellipticity at higher redshift. In particular, they find that  $\langle e \rangle = 0.33 + 0.05z$  for all of their halos, with slightly stronger evolution ( $d\langle e \rangle/dz = 0.06-0.07$ ) for their lowest mass halos, which overlap with our high mass halos (note that these authors define  $e \equiv 1 - b/a$ ). There are two possible interpretations for this result: either individual halos become more spherical with time, or halos that form later are intrinsically more spherical and the evolution seen by HBB05 is due to the growth of individual halos, resulting in a typically later formation time of halos of a given mass as time passes. It is interesting to compare this with the results of Bailin & Steinmetz (2004), who studied the evolution of the ellipticity of individual halos at  $z \approx 0$ . Bailin & Steinmetz (2004) find that individual halos have a mean  $d(b/a)/dt = 0.007$   $h^{-1}$   $\text{Gyr}^{-1}$ , corresponding to  $d\langle e \rangle/dz = 0.07$ , in good agreement with HBB05. We conclude that the shapes of individual halos become more spherical with time.

Weak lensing measurements have recently begun to probe the two-dimensional projected ellipticity of the lensing mass distribution (Hoekstra et al. 2004). For each halo in our sample, we have calculated the projected axis ratio  $q$  using the method of Stark (1977) for two random orientations, and calculated the ellipticity  $e$  using equation (1). A histogram of the results for the  $R = 0.4$   $r_{\text{vir}}$  shell is shown in Figure 6. The mean and median of the distribution of ellipticities are  $e_{\text{mean}} = 0.24$

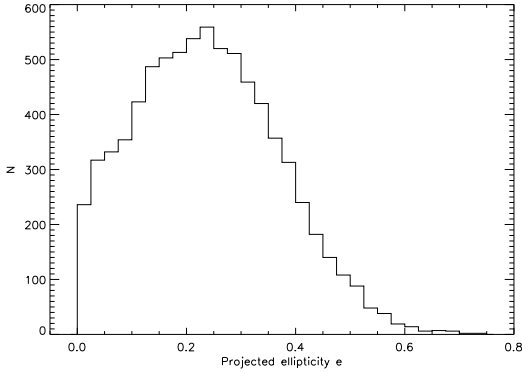


FIG. 6.— Projected ellipticity  $e$  of each halo seen from two random orientations, measured at  $R = 0.4 r_{\text{vir}}$ .

TABLE 1  
NUMBER OF HALOS WITH AXES DETERMINED TO WITHIN  
0.2 RADIANs

Radius ( $r_{\text{vir}}$ )	Major axis	Intermediate axis	Minor axis
0.06	904	388	621
0.12	2370	1005	1628
0.25	2942	1762	2540
0.4	2545	1488	2421
0.6	2322	1363	2324
1.0	2973	2231	2944

and  $e_{\text{median}} = 0.23$  respectively, with a  $1\sigma$  width of 0.13. This is consistent with the lower limit of  $\langle e \rangle = 0.33^{+0.07}_{-0.09}$  found by Hoekstra et al. (2004) from stacked weak lensing measurements around galaxies. It is smaller than the ellipticities found by Croft & Metzler (2000) (note that they quantify ellipticity as  $e = (1 - q^2)/(1 + q^2)$ , in which units our mean ellipticity is  $e = 0.27$ ). However, most of the halos used in their study have higher masses than the galactic-mass halos studied here, and they included relatively poorly-resolved halos which may skew the results toward higher ellipticities.

#### 4. INTERNAL ALIGNMENT

##### 4.1. Principal axes

We compare the alignment of the principal axes within each halo to see whether the approximation of the halo as a set of concentric ellipsoids is justified (JS02). In order to determine whether the axes are aligned, the directions of the axes must be well determined, otherwise apparent misalignments may be produced owing to measurement errors. Therefore, we restrict ourselves in this section to axes whose bootstrap error is less than 0.2 radians. The number of halos satisfying this criterion at each radius for each axis is given in Table 1.

To understand the effect of the error on the determination of the alignment, consider two axes which are intrinsically perfectly aligned, but are each measured with an error of 0.2 radians (note that this is the worst possible case — the median error of the sample is 0.1 radians). Due to the measurement error, these axes will appear to be misaligned by an angle  $\theta_{\text{spurious}}$ . The component

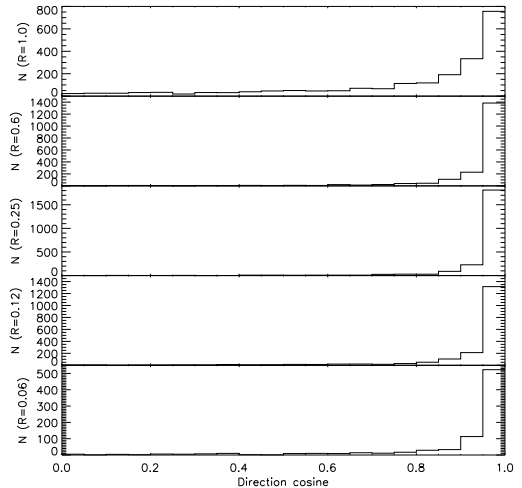


FIG. 7.— Histograms of the direction cosine between the major axis of the halo at  $R = 0.4 r_{\text{vir}}$  and the major axis at  $R = 1.0, 0.6, 0.25, 0.12,$  and  $0.06 r_{\text{vir}}$  (top to bottom). Due to the symmetry of the axes, this is always positive. Each histogram contains all halos where the major axes at both radii are determined to within 0.2 radians. If the axes were isotropic, this distribution would be uniform.

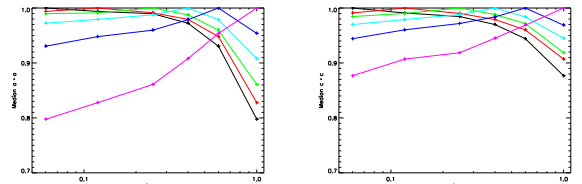


FIG. 8.— Median alignment of the major (*a-left*) and minor (*b-right*) axes at different radii. The alignment is with respect to the  $R = 0.06$  (black/solid),  $R = 0.12$  (red/dotted),  $R = 0.25$  (green/short-dashed),  $R = 0.4$  (cyan/dot-dashed),  $R = 0.6$  (blue/dot-dot-dot-dashed), and  $R = 1.0 r_{\text{vir}}$  (magenta/long-dashed) shell. For each pair of radii, only halos where the direction of the axis is determined to within 0.2 radians at both radii are used.

of an isotropic error in any particular plane, such as the plane containing both of the measured axes, is half of the isotropic error, so we divide the isotropic error of 0.2 radians by two and add the error of each axis in quadrature to find the typical  $\theta_{\text{spurious}} \approx 0.14$ . Therefore, the cosine of the angle between the two axes, which is intrinsically 1.0, is measured to be  $\cos \theta_{\text{spurious}} = 0.99$ . If the axes are intrinsically perpendicular, in which case the effect of  $\theta_{\text{spurious}}$  on the direction cosine is maximized, the error in the direction cosine is 0.14. Most halos have well aligned axes (see below), so the error is negligible.

Figure 7 shows histograms of the alignment between the major axis of the  $R = 0.4 r_{\text{vir}}$  shell and the major axis of the outer (top two panels) and inner (bottom three panels) regions of the halo. The alignment is very good at all radii. The relative alignment of the major and minor axes as a function of radius is shown in Figure 8. Each line shows the median alignment with respect to a different fiducial radius, recognizable as the radius where the median is exactly unity. The axes are extremely well aligned within  $0.6 r_{\text{vir}}$ . Near the virial radius, some ha-

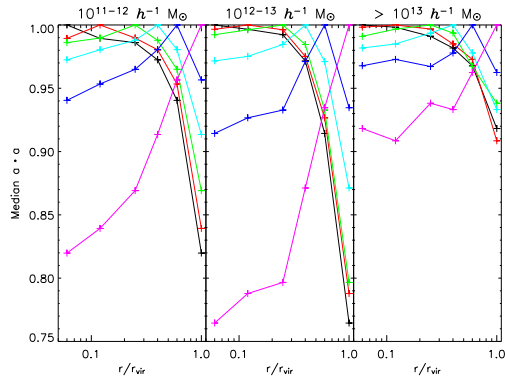


FIG. 9.— Median alignment of the major axis, as in Figure 8a, but only for halos with masses of  $10^{11} - 10^{12} h^{-1} M_{\odot}$  (left),  $10^{12} - 10^{13} h^{-1} M_{\odot}$  (middle), and  $10^{13} - 3 \times 10^{14} h^{-1} M_{\odot}$  (right). The alignment is with respect to the  $R = 0.06$  (black/solid),  $R = 0.12$  (red/dotted),  $R = 0.25$  (green/short-dashed),  $R = 0.4$  (cyan/dot-dashed),  $R = 0.6$  (blue/dot-dot-dashed), and  $R = 1.0 r_{\text{vir}}$  (magenta/long-dashed) shell. For each pair of radii, only halos where the direction of the axis is determined to within 0.2 radians at both radii are used.

los show deviations, but there is still usually very good alignment, especially for the minor axis. The alignment is better than that seen by JS02. This confirms their suggestion that many of the halos in which they measured poor alignment were nearly prolate or oblate. Such halos have large errors in their direction determination, and so are not included in our sample.

Figure 9 examines the internal alignment of the major axis as a function of halo mass. The inner  $0.4 r_{\text{vir}}$  of the halos are equally well aligned for halos of all masses. However, the outer half of the halo is better aligned with the rest of the halo in high mass halos than in low mass halos. JS02 saw a similar effect and suggested that it was because the low mass halos are intrinsically rounder and therefore have larger errors. We rule out this explanation, as halos with large errors are not included in our sample for any mass. Therefore, the stronger alignment within high mass halos appears to be a real effect.

#### 4.2. Angular momentum

Before we examine the orientation of the angular momentum, it is worth commenting on its magnitude in our simulated halos. The angular momentum is usually quantified by the spin parameter  $\lambda$ , where

$$\lambda \equiv \frac{J |E|^{1/2}}{GM^{5/2}} \quad (6)$$

(Peebles 1969). We use the computationally simpler  $\lambda'$  as an estimate for  $\lambda$ , where

$$\lambda' \equiv \frac{J}{\sqrt{2}MVR} \quad (7)$$

(Bullock et al. 2001a). In Figure 10, we plot the distribution of spin parameters for our halos. The thick line denotes the distribution we find when we use all of the mass inside  $r_{\text{vir}}$  to calculate  $\lambda$ . The spin parameters are well described by a lognormal distribution, shown as the dashed line:

$$P(\lambda) = \frac{1}{\lambda \sqrt{2\pi\sigma}} \exp\left(-\frac{\ln^2(\lambda/\lambda_0)}{2\sigma^2}\right), \quad (8)$$

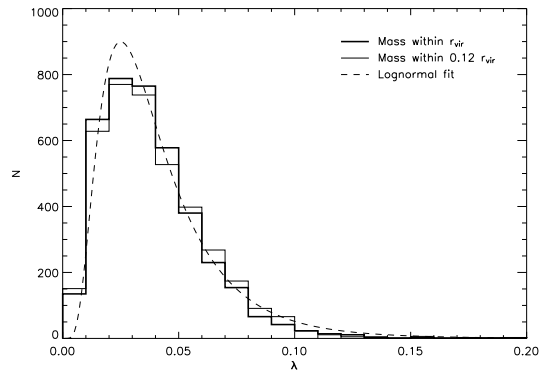


FIG. 10.— Histogram of spin parameters  $\lambda$  for the halos in our sample. The thick line shows the distribution when all of the mass in the halo is used to calculate  $\lambda$ , while the thin line shows the distribution when only the central  $0.12 r_{\text{vir}}$  of the halo is used. The dashed line is the lognormal fit to the distribution, where  $\lambda_0 = 0.035$  and  $\sigma = 0.58$ .

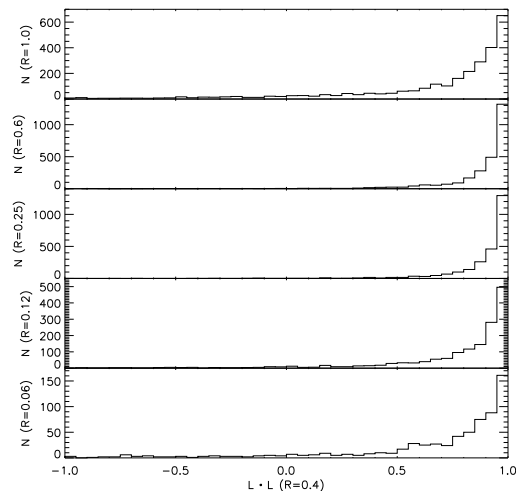


FIG. 11.— Histograms of the direction cosine between the angular momentum of the halo at  $R = 0.4 r_{\text{vir}}$  and the angular momentum at  $R = 1.0, 0.6, 0.25, 0.12,$  and  $0.06 r_{\text{vir}}$  (top to bottom). Each histogram contains halos whose angular momentum direction is determined to within 0.4 radians at both radii of the comparison. If the orientations were isotropic, this distribution would be uniform.

with  $\lambda_0 = 0.035$  and  $\sigma = 0.58$ , in good agreement with the results of other simulations (Bullock et al. 2001a). The distribution of spin parameters remains essentially unchanged if we only include mass within the central  $0.12 r_{\text{vir}}$  of the halo, as seen by the thin histogram in Figure 10, indicating that the angular momentum is distributed evenly throughout the halo. In the very innermost  $0.06 r_{\text{vir}}$ , the spin parameters rise, with the median value of  $\lambda$  increasing from  $\lambda_0 = 0.035$  to 0.047. However, we do not believe that this is a physical effect, as the particles in this region are affected by the numerical force softening, which results in more tangential orbits and correspondingly larger spin parameters.

The orientation of the angular momentum cannot be determined as precisely as the orientation of the principal axes. In order to have a reasonably large sample of halos,



TABLE 2  
NUMBER OF  
HALOS WITH  
ANGULAR  
MOMENTUM  
DIRECTIONS  
DETERMINED TO  
WITHIN  
0.4 RADIANs

Radius	Halos
0.06	702
0.12	1686
0.25	2820
0.4	3060
0.6	3094
1.0	3229

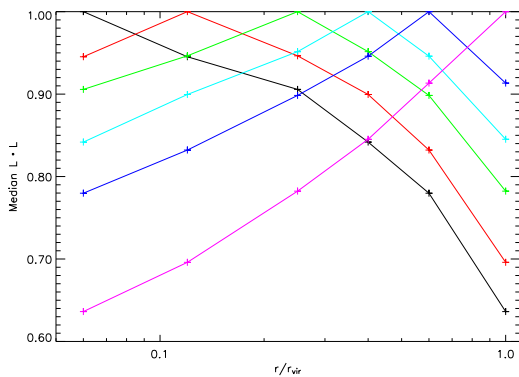


FIG. 12.— Median alignment of the angular momentum vector at different radii. The alignment is with respect to the  $R = 0.06$  (black/solid),  $R = 0.12$  (red/dotted),  $R = 0.25$  (green/short-dashed),  $R = 0.4$  (cyan/dot-dashed),  $R = 0.6$  (blue/dot-dot-dot-dashed), and  $R = 1.0 r_{\text{vir}}$  (magenta/long-dashed) shell. For each pair of radii, only halos where the direction of the angular momentum vector is determined to within 0.4 radians at both radii are used.

we use angular momentum vectors whose bootstrap error is less than 0.4 radians. This is twice as large as the limit adopted for the principal axis directions. The number of halos that satisfy this criterion at each radius is given in Table 2. Following the logic of § 4.1, the error in the direction cosine of two vectors with errors of 0.4 radians is 0.04 if they are perfectly aligned and 0.28 if they are perpendicular. The median errors of the samples are half of these worst-case scenarios. The alignment is shown to be good (see below), so the effect of the errors is negligible.

Figure 11 shows histograms of the relative alignment of the angular momentum of the  $R = 0.4 r_{\text{vir}}$  shell with the outer regions of the halo (upper two panels) and the inner regions of the halo (lower three panels). The alignment is very good at most radii.

The relative alignment of the angular momentum as a function of radius is shown in Figure 12. Each line shows the median alignment of the angular momentum with respect to a different fiducial radius, recognizable as the radius where the median is exactly unity. The alignment gets progressively worse as the radii get further separated; the median cosine between the angular momenta in the innermost and outermost regions is 0.64.

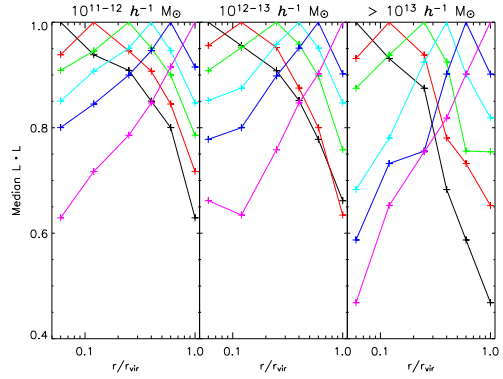


FIG. 13.— Median angular momentum alignment as in Figure 12, but only for halos with masses of  $10^{11} - 10^{12} h^{-1} M_{\odot}$  (left),  $10^{12} - 10^{13} h^{-1} M_{\odot}$  (middle), and  $10^{13} - 3 \times 10^{14} h^{-1} M_{\odot}$  (right). The alignment is with respect to the  $R = 0.06$  (black/solid),  $R = 0.12$  (red/dotted),  $R = 0.25$  (green/short-dashed),  $R = 0.4$  (cyan/dot-dashed),  $R = 0.6$  (blue/dot-dot-dot-dashed), and  $R = 1.0 r_{\text{vir}}$  (magenta/long-dashed) shell. For each pair of radii, only halos where the direction of the angular momentum vector is determined to within 0.4 radians at both radii are used.

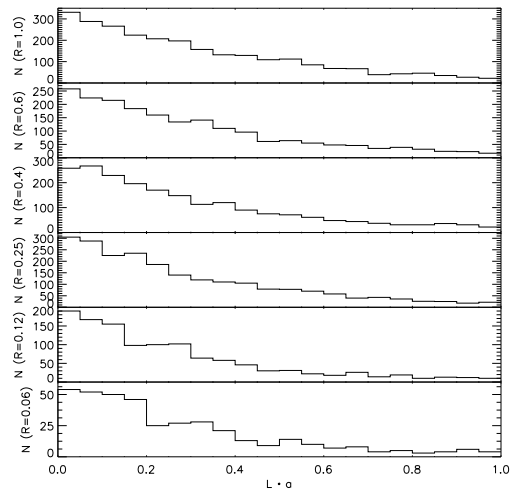


FIG. 14.— Histograms of the alignment between the angular momentum vector and the major axis of the  $R = 1.0, 0.6, 0.4, 0.25, 0.12,$  and  $0.06 r_{\text{vir}}$  (top to bottom) shell of each halo where the error in the major axis direction is less than 0.2 radians and the error in the angular momentum direction is less than 0.4 radians at that radius. Due to the symmetry of the axes, the direction cosine is always positive. If the orientations were random, this distribution would be uniform.

However, the angular momentum vector at intermediate radius, such as at  $0.4 r_{\text{vir}}$ , is generally representative of its direction at all radii.

Figure 13 examines the internal alignment of the angular momentum as a function of halo mass. The patterns seen in Figure 12 generally hold for all masses, although the alignment between the very innermost and outermost regions is slightly worse for the highest mass halos.

#### 4.3. Alignment between the angular momentum and the halo shape

We investigate here the alignment between the angular momentum of a halo at a given radius and the principal

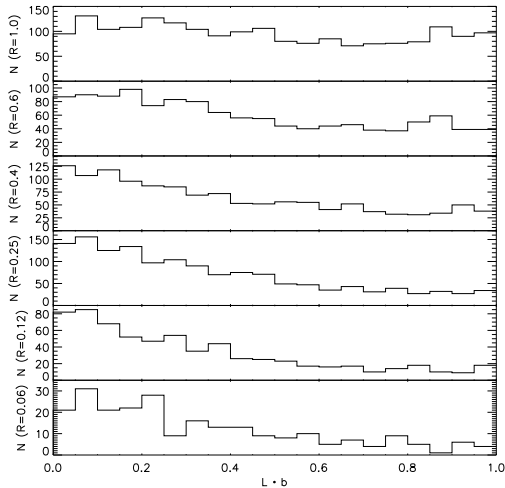


FIG. 15.— As in Figure 14 but for the intermediate axis.

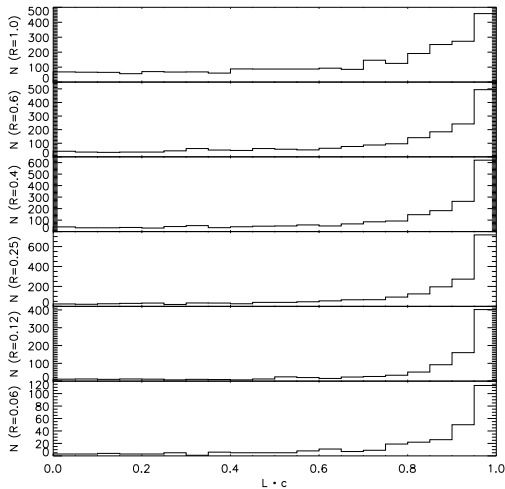


FIG. 16.— As in Figures 14 and 15 but for the minor axis.

axes of the mass distribution at that radius. If we compare an angular momentum vector whose error is 0.4 radians with a principal axis whose error is 0.2 radians, the error in the direction cosine is 0.02 if they are perfectly aligned and 0.22 if they are perpendicular. The median errors are half of those values. Therefore, in the cases where the alignment is good, the effect of the errors is negligible. In the cases where the vectors are perpendicular or isotropic, we must take the errors into account when drawing conclusions.

Figures 14, 15, and 16 show histograms of the cosine between the direction of the angular momentum vector and the major, intermediate, and minor axis respectively. Only those halos with both angular momentum direction errors of less than 0.4 radians and axis direction errors of less than 0.2 radians are used. The angular momentum vector tends to be perpendicular to the major and inter-

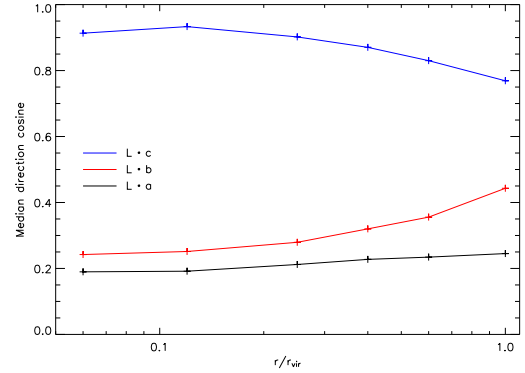
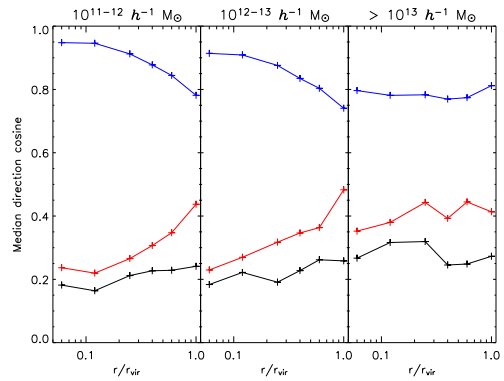


FIG. 17.— Median alignment between the angular momentum vector and the major (black/solid), intermediate (red/dotted), and minor (blue/dashed) axis of each halo as a function of radius within the halo.

FIG. 18.— As in Figure 17, but only for halos with masses of  $10^{11} - 10^{12} h^{-1} M_{\odot}$  (left),  $10^{12} - 10^{13} h^{-1} M_{\odot}$  (middle), and  $10^{13} - 3 \times 10^{14} h^{-1} M_{\odot}$  (right).

mediate axes, and parallel with the minor axis. Because of the different effects of the error on parallel and perpendicular vectors, the tendency of the angular momentum to be perpendicular to the major axis is as significant as the trend for it to be parallel to the minor axis, despite the different appearance of the histograms. The angular momentum tends to lie perpendicular to the intermediate axis, but this trend is weaker at larger radii.

These results are consistent with those of Barnes & Efstathiou (1987), Dubinski (1992), and W92. Of these, only W92 quantify any change with radius; they found slightly better alignment at larger radii, in contrast to the results presented here. However, both of the radii at which they performed the comparison were well within the virial radius, well inside the radii where we see the alignment drop.

These relationships are summarized in Figure 17, which shows the median alignment between the angular momentum vector and each of the principal axes. The angular momentum tends to lie parallel with the minor axis and perpendicular to both the major and intermediate axes. These trends are strongest in the central  $0.25 r_{\text{vir}}$  of the halo, deteriorating slightly in the outer regions. The median cosine of 0.9 corresponds to a misalignment between the angular momentum and minor axis of  $25^{\circ}$ . Figure 18 shows how these trends depend

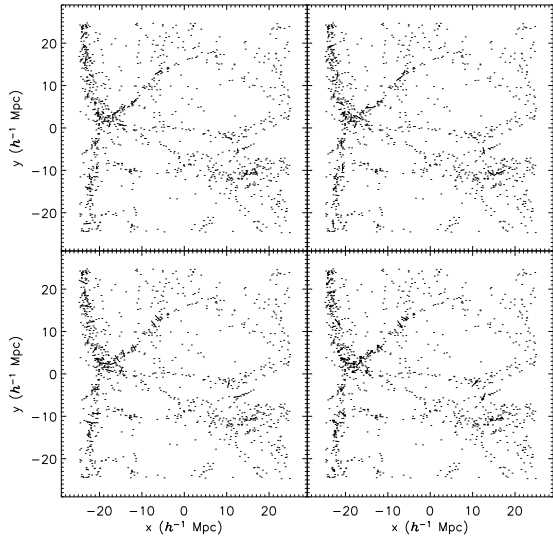


FIG. 19.— Projection in  $xy$  of the major (*top-left*), intermediate (*top-right*), and minor (*bottom-left*) axes, and unit angular momentum vectors (*bottom-right*) of high mass ( $M > 10^{13} h^{-1} M_{\odot}$ ) halos in a slab of depth  $\Delta z = 12.5 h^{-1} \text{ Mpc}$  (one quarter of the simulation volume). The three-dimensional length of each line or vector is  $2 h^{-1} \text{ Mpc}$ , including the unseen  $z$  component. Dots show the positions of all halos, regardless of mass.

on the halo mass. For high mass halos, the alignment is slightly worse and has less of a dependence on the location within the halo.

## 5. EXTERNAL ALIGNMENT

### 5.1. Introduction

In this section, we compare the orientation of the principal axes and angular momenta of individual halos with the location of mass around them and the orientation of those properties in surrounding halos. In § 4 we demonstrated that the properties of halos in the  $R = 0.4 r_{\text{vir}}$  shell are characteristic of their properties over a large range of radii. Therefore, we use the  $R = 0.4 r_{\text{vir}}$  measurements when comparing to other halos.

For each halo, the volume is split into 7 radial bins. The nearest bin spans separations from 0 to  $390.625 h^{-1} \text{ kpc}$ . The outer radii double for each subsequent bin, while the inner radius is equal to the outer radius of the interior bin. The largest bin has an outer radius of  $25 h^{-1} \text{ Mpc}$ , extending to the edge of the periodic box. The nominal radius of each bin is the outer radius divided by  $\sqrt{2}$ ; this corresponds to the geometric mean between its inner and outer radius for all but the innermost bin. The inner bin has no formal inner radius, but in practice is limited by twice the radial extent of the typical halo, or  $250 h^{-1} \text{ kpc}$ . Halos whose centers of mass are closer to each other than this are merging, and are detected as a single object by the group finder.

We follow the nomenclature of Splinter et al. (1997), and use “alignment” to refer to the tendency of a vector (such as a principal axis or an angular momentum vector) to point toward or away from other halos, and “correlation” to refer to the tendency of vectors in different halos to point in the same direction.

A visual impression of how the axes and angular momenta align can be seen in Figure 19, which shows the

axes and angular momentum vectors of the high mass halos ( $M > 10^{13} h^{-1} M_{\odot}$ ), with the location of the other halos shown as dots. Because of the filamentary nature of the large scale structure (e.g. Colberg et al. 1999), positive alignment indicates that a quantity tends to point along filaments.

### 5.2. Axis alignments

We compare here the alignment of the principal axes of the halos with the location of surrounding structure. Methods of measuring these alignments vary in the literature, as does the nomenclature for a given metric. We adopt an internally-consistent nomenclature  $\xi_{xy}$  and  $\xi_{|xy|}$ , which are defined to be the mean value of the direction cosine between direction  $x$  and direction  $y$ , and the mean of the absolute value of the direction cosine respectively. In general,  $\xi_{xy}$  is positive if  $x$  and  $y$  point in the same direction and negative if they point in opposite directions (this is not applicable if  $x$  or  $y$  is symmetric, such as if it is a principal axis), while  $\xi_{|xy|}$  is greater than  $1/2$  if  $x$  and  $y$  lie parallel to each other and less than  $1/2$  if they lie perpendicular to each other. We note names other authors use for the same quantities when applicable. For example, to measure the alignment of the major axis, whose direction is defined by the unit vector  $\hat{\mathbf{a}}$ , with the large scale structure, we calculate the alignment  $\xi_{|ar|}$ :

$$\xi_{|ar|}(r) \equiv \langle |\hat{\mathbf{a}} \cdot \hat{\mathbf{r}}| \rangle \equiv \frac{1}{N} \sum_{i,j} |\hat{\mathbf{a}}_i \cdot \hat{\mathbf{r}}_{ij}|, \quad (9)$$

where the sum over  $i$  is over all halos in the primary sample, the sum over  $j$  is over all halos in the secondary sample,  $\hat{\mathbf{r}}_{ij}$  is a unit vector in the direction of the displacement from halo  $i$  to halo  $j$ , and  $N$  is the number of terms in the double sum. The primary sample consists of all halos whose major axis is determined to within  $0.2$  radians, while the secondary sample consists of all halos. We define the alignments  $\xi_{|br|}$  and  $\xi_{|cr|}$  for the intermediate axis  $\hat{\mathbf{b}}$  and the minor axis  $\hat{\mathbf{c}}$  similarly. Note that the primary samples used to define  $\xi_{|ar|}$ ,  $\xi_{|br|}$ , and  $\xi_{|cr|}$  are not identical, as the set of halos with good major axis determinations is deficient in very oblate halos, the set of halos with good minor axis determinations is deficient in very prolate halos, and the set of halos with good intermediate axis determinations is deficient in both very prolate and very oblate halos.

Figure 20 shows histograms of the distribution of direction cosines  $|\hat{\mathbf{a}} \cdot \hat{\mathbf{r}}|$  for halos at a variety of separations. If the axes were randomly oriented, the distributions would be uniform. The distribution is mostly isotropic, but there is an excess of halos with  $|\hat{\mathbf{a}} \cdot \hat{\mathbf{r}}| > 1/2$ , i.e. halos whose major axes lie parallel to the filaments. We quantify this by calculating the mean,  $\xi_{|ar|}$  (note that this is similar but not identical to the quantity  $w(r)$  used by KE04).

The upper-left panel of Figure 21 shows  $\xi_{|ar|}$  for the halos. We find that the alignment is well fit by a power law over a wide range of separations. The fit is shown as the solid line in Figure 21, and is given by

$$\xi_{|ar|}(r) = \frac{1}{2} + m_1 r^\alpha, \quad (10)$$

where  $r$  is the separation in units of  $h^{-1} \text{ Mpc}$ , the alignment at  $1 h^{-1} \text{ Mpc}$  is  $m_1 = 0.015$ , and the slope is

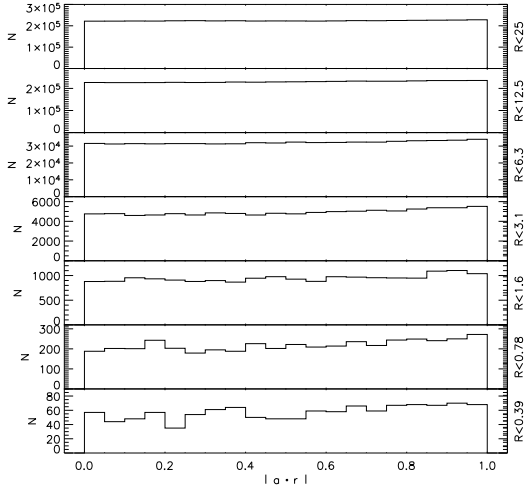


FIG. 20.— Histograms of the direction cosine  $|\hat{\mathbf{a}} \cdot \hat{\mathbf{r}}|$  between the major axes of halos in the primary sample and the displacement from each primary halo to all surrounding halos, binned by radial separation between the centers of the halos. The direction cosine is always positive due to the symmetry of the axes. If the axes were randomly oriented, the distributions would be uniform. The radial bins consist of halos separated by (top to bottom): 12.5 – 25, 6.25 – 12.5, 3.125 – 6.25, 1.5625 – 3.125, 0.78125 – 1.5625, 0.390625 – 0.78125, and 0 – 0.390625  $h^{-1}$  Mpc respectively.

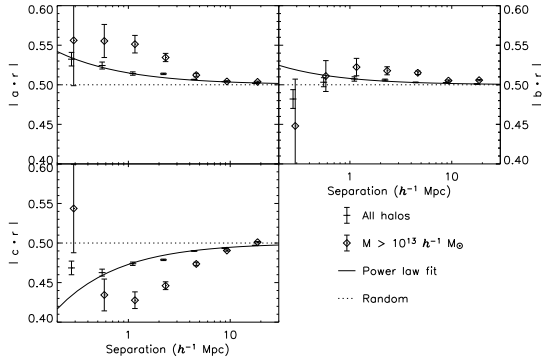


FIG. 21.— Mean alignment of the principal axes of halos in the primary sample with the displacement from the primary halos to all surrounding halos, as a function of distance between the halos. The alignment of the major axis ( $\xi_{|ar|}$ ), intermediate axis ( $\xi_{|br|}$ ), and minor axis ( $\xi_{|cr|}$ ) is plotted in the top-left, top-right, and bottom-left panels respectively. Only halos where the relevant axis is determined to within 0.2 radians are used for the primary sample. The different symbols are for primary samples consisting of all such halos (crosses) or of only those with masses greater than  $10^{13} h^{-1} M_{\odot}$  (diamonds). The diamonds are shifted slightly to the right for clarity. Error bars represent the  $1\sigma$  Poisson sampling error in the mean. The solid lines are the power law fits for the full samples, and are given by equations (10), (11), and (12). The dotted line is the value expected for random orientations.

$\alpha = -0.64$ . F02 find even stronger alignment for their cluster-mass halos, as do KE04 and HBB05 (except at the very smallest separations, which is at the spatial limit of their simulations and the point where halos begin to overlap). This may be because all of these authors analyze simulations performed in much larger boxes, which contain power on longer wavelengths than exist in our

smaller simulation volume (which also allows them to measure alignments at separations far exceeding our entire box length). Alternatively, the stronger alignment they detect may be a consequence of the higher mass of their halos. To see whether the halo mass is important, we recalculate  $\xi_{|ar|}$ , restricting the primary sample to those halos with masses greater than  $10^{13} h^{-1} M_{\odot}$ . This is the tendency for the major axes of group or cluster mass halos to point along the filaments. The results are shown as the diamonds in Figure 21. The group and cluster mass halos are much more strongly aligned than the full sample (which is dominated by galaxy mass halos). The cluster alignment  $\xi_{|ar|}$  is constant out to  $3 h^{-1}$  Mpc, after which it drops until it agrees with the results of the full sample by  $6 h^{-1}$  Mpc. HBB05 also find a strong mass dependence; however, the alignments of their lowest mass sample are still larger than the alignments of our highest mass sample, indicating that the box size also plays a role.

The intermediate axes are also aligned with the filaments, as seen in the upper-right panel of Figure 21. While the innermost bins show no alignment, there is clear evidence of alignment at separations of  $1 h^{-1}$  Mpc and beyond. The solid line is a power law fit to the outer 5 points, i.e. for  $r > 781 h^{-1}$  kpc, and is given by

$$\xi_{|br|} = \frac{1}{2} + m_1 r^{\alpha}, \quad (11)$$

where  $m_1 = 0.008$  and  $\alpha = -0.7$ . The high mass halos again show constant alignment out to several Mpc.

As both the major and intermediate axes tend to point along filaments, the minor axis must tend to lie perpendicular to the filaments. This trend can be clearly seen in the bottom-left panels of Figure 19 as sequences of parallel lines crossing the filaments. The lower panel of Figure 21 shows  $\xi_{|cr|}$ . The solid line is a power law fit for the full sample excluding the innermost bin, i.e. for  $r > 391 h^{-1}$  kpc, and is given by

$$\xi_{|cr|}(r) = \frac{1}{2} + m_1 r^{\alpha}, \quad (12)$$

where the alignment at  $1 h^{-1}$  Mpc is  $m_1 = -0.027$  and  $\alpha = -0.7$ . The minor axes of group and cluster mass halos show even stronger alignment than do the galaxy mass halos, as seen by the diamonds in Figure 21.

### 5.3. Axis correlations

We compare here the tendency for the principal axes of neighbouring halos to point in the same direction. The procedure we use is completely analogous to that used to calculate the alignments in § 5.2. The correlation between the major axes is defined as

$$\xi_{|aa|}(r) \equiv \langle |\hat{\mathbf{a}} \cdot \hat{\mathbf{a}}| \rangle \equiv \frac{1}{N} \sum_{i,j} |\hat{\mathbf{a}}_i \cdot \hat{\mathbf{a}}_j|, \quad (13)$$

where the sum is over all unique pairs  $(i, j)$  because the measurement is symmetric with respect to each pair of halos. Only halos whose major axes are determined to within 0.2 radians are used for both the primary and secondary samples.

The top-left panel of Figure 22 shows the mean correlation  $\xi_{|aa|}$  of the major axes as a function of the halo separation (this is identical to the quantity defined as

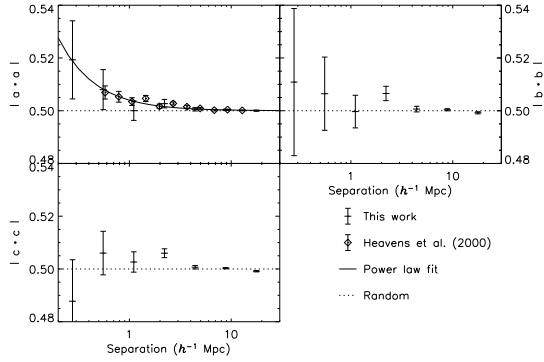


FIG. 22.— Mean correlation of the principal axes of halos for which the direction of the major axes is determined to within 0.2 radians for both halos. The correlations of the major axes ( $\xi_{|aa|}$ ), intermediate axes ( $\xi_{|bb|}$ ), and minor axes ( $\xi_{|cc|}$ ) are plotted in the upper-left, upper-right, and bottom-left panels respectively. The solid line is the power law fit for the major axis correlation, and is given by equation (14). The dotted line is the expected value for random orientations. Error bars represent the  $1\sigma$  Poisson sampling error in the mean. Diamonds represent the results of HRH00.

$u(r)$  in KE04). Although almost all bins are individually consistent with isotropy, they all lie above 0.5, and taken together are evidence that the directions of the major axes are correlated. We fit a power law and find

$$\xi_{|aa|}(r) = \frac{1}{2} + m_1 r^\alpha, \quad (14)$$

where  $r$  is the separation in units of  $h^{-1}$  Mpc, the correlation at  $1 h^{-1}$  Mpc is  $m_1 = 0.004$ , and the slope is  $\alpha = -1.2$ , although the large errors introduce considerable uncertainties in these values. The correlations found by F02, KE04 and HBB05 are considerably stronger than those found here. Comparison with the results of Croft & Metzler (2000) and HRH00 is more difficult because these authors measure projected ellipticity correlations rather than axis correlations. The ellipticity correlations are diluted with respect to the axis correlations, and therefore we should consider their results as lower limits. The results of HRH00 are plotted as diamond in Figure 14, where we note that

$$\xi_{|aa|} = \frac{1}{2} + \frac{\sqrt{3}}{2} (\langle e_1 e_1 \rangle + \langle e_2 e_2 \rangle). \quad (15)$$

The agreement is excellent. However, because their results should be considered as lower limits, and Croft & Metzler (2000) found even larger ellipticity correlations in the same simulation, it appears that the shapes of the halos studied by these authors also correlate more strongly than the halos in our simulation. This is likely because our sample is dominated by galaxy mass halos, while all of the previous studies have analyzed only cluster mass halos. We have demonstrated in § 5.2 that the higher mass halos are more strongly aligned with the large scale structure; it is therefore likely that they also show stronger correlations with each other. To test this, we have recalculated  $\xi_{|aa|}$  using only halos with masses greater than  $10^{13} h^{-1} M_\odot$  to see if the behaviour of high mass halos differs from those of lower mass, but due to the small number of very high mass halos in our sample, the errors are too large to draw any conclusions.

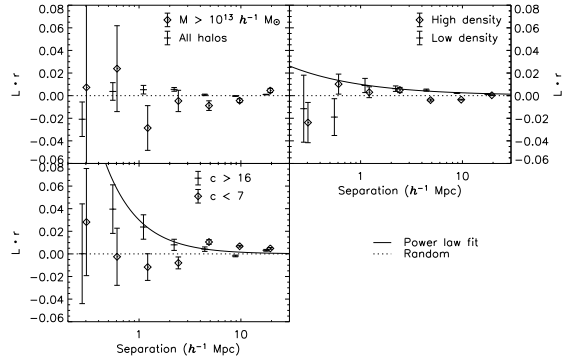


FIG. 23.— Mean vector alignment  $\xi_{LR}$  between the angular momentum vector of a halo and the location of surrounding halos, as a function of radial separation. Error bars represent the  $1\sigma$  Poisson sampling error in the mean. The dotted line is the expected value for random orientations. Diamonds are shifted to the right for clarity. (Top-left): The alignment of all halos (crosses), and of only those halos with masses greater than  $10^{13} h^{-1} M_\odot$  (diamonds). (Top-right): The alignment of halos that have 3 or fewer neighbouring halos within  $2 h^{-1}$  Mpc (crosses) compared to those halos with 4 or more neighbouring halos within  $2 h^{-1}$  Mpc (diamonds). The solid line is the power law fit for the low density sample at  $r > 781 h^{-1}$  kpc, and is given by equation (17) with  $m_1 = 0.01$  and  $\alpha = -0.6$ . (Bottom-left): The alignment of halos with concentration parameter  $c_{\text{vir}} > 16$  (crosses) compared to those with NFW concentration parameter  $c_{\text{vir}} < 7$  (diamonds). The solid line is the power law fit for the high concentration sample at  $r > 391 h^{-1}$  kpc, and is given by equation (17) with  $m_1 = 0.03$  and  $\alpha = -1.3$ .

The mean correlations of the intermediate and minor axes of the halos,  $\xi_{|bb|}$  and  $\xi_{|cc|}$ , are plotted in the upper-right and lower-left panels of Figure 22. The error bars are too large to robustly detect any correlation, though the lower panel shows a suggestive preponderance of bins with  $\xi_{|cc|} > 0.5$ . A larger sample of halos simulated at equally high spatial resolution is required to confirm if this is real.

#### 5.4. Angular momentum

We investigate the tendency for the angular momentum to point toward or away from nearby halos, for it to lie parallel or perpendicular to the filamentary structure, and for the angular momentum vectors of neighbouring halos to point in the same direction. To measure the tendency of halo angular momenta to point toward or away from other halos, we calculate the alignment

$$\xi_{LR}(r) \equiv \langle \hat{\mathbf{L}} \cdot \hat{\mathbf{r}} \rangle \equiv \frac{1}{N} \sum_{i,j} \hat{\mathbf{L}}_i \cdot \hat{\mathbf{r}}_{ij}, \quad (16)$$

where  $\hat{\mathbf{L}}_i$  is a unit vector in the direction of the angular momentum vector for halo  $i$ . The primary sample consists of all halos where the direction of the angular momentum is determined to within 0.4 radians, while the secondary sample consists of all halos. We show the results in the top-left panel of Figure 23. There may be a weak tendency for the angular momentum to point toward local density enhancements on scales of  $0.5 - 3 h^{-1}$  Mpc, but the size of the error bars makes such a result tentative. When we restrict the sample to those halos with masses greater than  $10^{13} h^{-1} M_\odot$ , we find no statistical deviation from random.

Kashikawa & Okamura (1992) and Navarro et al. (2004) have found that galaxies within the local supercluster have their spins pointing within the supercluster plane, while those at least  $2 h^{-1}$  Mpc from the plane have spins that point toward or away from the plane. To see if the behaviour of simulated halos in low and high density regions differs, we have split the sample into those halos that have 3 or fewer neighbouring halos within  $2 h^{-1}$  Mpc (the low density sample), and those that have 4 or more neighbours within  $2 h^{-1}$  Mpc (the high density sample). There are 2155 and 1714 halos in the low and high density samples respectively. In the top-right panel of Figure 23 we have plotted  $\xi_{Lr}$  for these two samples. By construction, there are very few pairs (and therefore large error bars) at small separations in the low density sample, but beyond  $1 h^{-1}$  Mpc there is a clear detection of positive alignment in this sample. The alignment is well fit by a power law of the form

$$\xi_{Lr} = m_1 r^\alpha, \quad (17)$$

where  $r$  is the separation in units of  $h^{-1}$  Mpc, the correlation at  $1 h^{-1}$  Mpc is  $m_1 = 0.01$ , and the slope is  $\alpha = -0.6$ . The high density sample shows no coherent tendency for the angular momentum vectors to point toward or away from density enhancements. The low and high density samples do not show significant deviations from the full sample for any of the other statistics studied.

In order to see how the internal structure of the halo affects its alignment properties, we have split the sample into those halos with particularly high NFW (Navarro et al. 1996) concentration parameters ( $c_{\text{vir}} > 16$ ) and those with particularly low concentration parameters ( $c_{\text{vir}} < 7$ ). As demonstrated by the bottom-left panel of Figure 23, there is a clear signal of positive alignment in the high-concentration sample, and none in the low-concentration sample. The alignment of the high-concentration sample is well fit by a power law of the form of equation (17), with  $m_1 = 0.03$  and  $\alpha = -1.3$ . Because halo concentration anti-correlates with mass (Bullock et al. 2001b), our high-mass sample is deficient in high-concentration halos. Therefore, the tendency for low mass halos to show positive  $\xi_{Lr}$  while high mass halos show no such a tendency is probably a direct consequence of the correlation between  $\xi_{Lr}$  and  $c_{\text{vir}}$ .

The tendency for the angular momentum vectors to lie parallel versus perpendicular to the filaments is measured by

$$\xi_{|Lr|}(r) \equiv \langle |\hat{\mathbf{L}} \cdot \hat{\mathbf{r}}| \rangle \equiv \frac{1}{N} \sum_{i,j} |\hat{\mathbf{L}}_i \cdot \hat{\mathbf{r}}_{ij}|, \quad (18)$$

defined as  $L_{\parallel}$  in Hatton & Ninin (2001), or

$$\omega(r) \equiv \langle |\hat{\mathbf{L}} \cdot \hat{\mathbf{r}}|^2 \rangle - \frac{1}{3} \equiv \frac{1}{N} \sum_{i,j} |\hat{\mathbf{L}}_i \cdot \hat{\mathbf{r}}_{ij}|^2 - \frac{1}{3}, \quad (19)$$

as used by Lee & Pen (2001). We plot these quantities in Figure 24. The solid line in the bottom panel shows the prediction of Lee & Pen (2001) from linear tidal torque theory. On scales less than  $3 h^{-1}$  Mpc, the angular momentum tends to lie parallel to the filaments. The values are consistent with those found by Hatton & Ninin (2001). However, both Lee & Pen

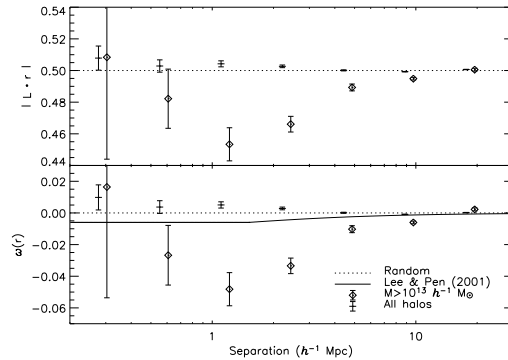


FIG. 24.— Mean alignment  $\xi_{|Lr|}$  (top) and  $\omega(r)$  (bottom) between the angular momentum vector of primary halos and the location of all surrounding halos. The different symbols are for primary samples consisting of all such halos (crosses), or of only those with masses greater than  $10^{13} h^{-1} M_{\odot}$  (diamonds). The diamonds are shifted slightly to the right for clarity. Error bars represent the  $1\sigma$  Poisson sampling error in the mean. The dotted line is the expected value for random orientations. The solid line is the prediction from linear tidal torque theory (Lee & Pen 2001).

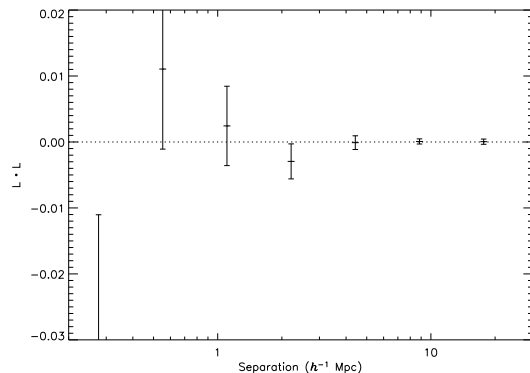


FIG. 25.— Mean correlation  $\xi_{LL}$  of the angular momentum vectors of halos as a function of their separation. Error bars represent the  $1\sigma$  Poisson sampling error in the mean. The dotted line is the expected value for random orientations.

(2001) and F02 find that the angular momenta of halos tend to lie perpendicular to the filaments. This discrepancy may lie in the different mass ranges probed. The halos of Hatton & Ninin (2001) cover a very similar mass range to those in this work, while the sample of F02 consists entirely of cluster mass halos (their *smallest* halo has a mass of  $1.4 \times 10^{14} h^{-1} M_{\odot}$ , nearly the mass of our *largest* halo). We have recalculated  $\xi_{|Lr|}$  and  $\omega(r)$  using only halos with masses greater than  $10^{13} h^{-1} M_{\odot}$  in the primary sample and plotted them as diamonds in Figure 24. The behaviour of the high mass halos is radically different; the angular momenta of groups and clusters tend to point perpendicular to the filaments.

The correlation between the directions of the halo angular momenta is defined as

$$\xi_{LL} \equiv \langle \hat{\mathbf{L}} \cdot \hat{\mathbf{L}} \rangle \equiv \frac{1}{N} \sum_{i,j} \hat{\mathbf{L}}_i \cdot \hat{\mathbf{L}}_j, \quad (20)$$

where the sum is over all unique pairs  $(i, j)$ . This is equivalent to the quantity defined is  $\eta(r)$  in Porciani et al. (2002a). As seen in Figure 25, we detect

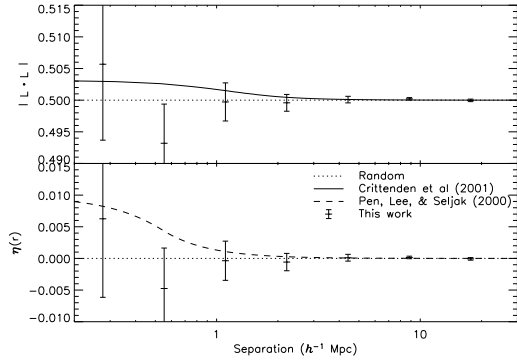


FIG. 26.— Mean correlation  $\xi_{|LL|}$  (*top*) and  $\eta(r)$  (*bottom*) between the angular momentum vectors of halos as a function of their separation. Error bars represent the  $1\sigma$  Poisson sampling error in the mean. The solid line shows the analytic result of Crittenden et al. (2001), where we set the correlation parameter between the shear and inertia tensors  $a = 0.55$ , while the solid line is the linear tidal torque prediction of Pen et al. (2000). The dotted line is the expected value for random orientations.

no deviations from random. We also measure the tendency for halo angular momentum vectors to be either parallel or perpendicular to each other. We define two quantities to measure this,

$$\xi_{|LL|} \equiv \langle |\hat{\mathbf{L}} \cdot \hat{\mathbf{L}}| \rangle \equiv \frac{1}{N} \sum_{i,j} |\hat{\mathbf{L}}_i \cdot \hat{\mathbf{L}}_j|, \quad (21)$$

which is the same as the quantity defined as  $\mu(r)$  in Hatton & Ninin (2001), and

$$\eta(r) \equiv \langle |\hat{\mathbf{L}} \cdot \hat{\mathbf{L}}|^2 \rangle - \frac{1}{3} \equiv \frac{1}{N} \sum_{i,j} |\hat{\mathbf{L}}_i \cdot \hat{\mathbf{L}}_j|^2 - \frac{1}{3}, \quad (22)$$

which is the same as Pen et al. (2000)'s  $\eta(r)$  and Porciani et al. (2002a)'s  $\eta_2(r)$ . The quantities  $\xi_{|LL|}(r)$  and  $\eta(r)$  are shown in Figure 26. We detect no deviations from isotropy. For reference, we also plot the linear predictions of Crittenden et al. (2001) (where we set the correlation parameter between the shear and inertia tensors  $a = 0.55$  so that the linear results also match the  $N$ -body results of HRH00) and Pen et al. (2000). Due to the size of the error bars, our results are consistent with the non-detections and weak correlations found by other authors (HRH00; Pen et al. 2000; Crittenden et al. 2001; Hatton & Ninin 2001; Porciani et al. 2002a; F02). The number of halos in our sample is too small to detect angular momentum correlations in any particular sub-sample.

## 6. DISCUSSION

### 6.1. Internal alignment and galactic warps

The internal alignment of the angular momentum provides several clues to the forces a galaxy undergoes during its evolution. In particular, we note that, as demonstrated in Figure 17, the angular momentum and the minor axis of a halo are typically misaligned by  $\sim 25^\circ$ , even in the central regions of the halo where a galactic disk would lie. Therefore, if the angular momentum of the dark matter and baryons are aligned, and the disk lies perpendicular to its angular momentum, then the disk

and halo will be typically misaligned by  $\sim 25^\circ$ . Such misalignment could be partly responsible for warped galactic disks (Dekel & Shlosman 1983; Toomre 1983; Bailin 2004). However, simulations of live disks in live halos demonstrate that misaligned disk-halo systems quickly reach an unwarped realigned equilibrium (Binney et al. 1998).

However, if the orientation of the disk and/or the orientation of the halo changes, then such an equilibrium may never be established. Quinn & Binney (1992) suggested that the infalling angular momentum may be uncorrelated with the orientation of the central angular momentum. Figure 12 demonstrates that this is true in our halos; while the angular momentum at intermediate radius is generally representative of its orientation at all radii, the angular momentum of the innermost and outermost regions are nearly uncorrelated. Therefore, as the disk accretes angular momentum, its orientation changes. This reorientation of the disk may itself cause warps (Ostriker & Binney 1989; López-Corredoira et al. 2002), or simply prevent the disk and halo from reaching an aligned equilibrium. Similarly, Bailin & Steinmetz (2004) found that over 90% of dark matter halos show figure rotation; this reorientation of the halo also acts to maintain misalignment between the disk and halo. Therefore, it appears that misalignment between the halo and disk is common, and perhaps responsible for galactic warps.

### 6.2. External alignment

The alignment of the halo axes with the large scale structure seen in Figure 21 provides several clues to the origin of halo orientations. For instance, the relative alignment of the major, intermediate, and minor axes is intriguing. The relative strength of the alignment is well described by  $m_1$ , the value of the power law fit at a separation of  $1 h^{-1}$  Mpc. This is 0.015, 0.008, and -0.027 for the major, intermediate, and minor axes respectively. While all previous authors have neglected the minor axis, we find that its alignment perpendicular to filaments is stronger than the alignment of the major axis along filaments. Therefore it is the minor axis, not the major axis, that is most influenced by the presence of surrounding material. This also explains how both the major and intermediate axes can be positively aligned with the filament: if the minor axis of a halo lies perpendicular to the filament, then both the major and intermediate axes are constrained to lie within a plane that contains the filament. Therefore, they are both more likely to point along the filament than a randomly-oriented three-dimensional axis, and therefore both show positive alignment (for example, if all of the minor axes were perfectly perpendicular to the filament and there were no difference between the major and intermediate axes, then  $\xi_{|cr|}$  would vanish and both  $\xi_{|ar|}$  and  $\xi_{|br|}$  would equal  $2/\pi \approx 0.64$ ). The geometry of the environment is not strictly linear, especially at larger scales. However, despite these complications, the relationships we have found provide useful quantitative predictions that can be tested when full three-dimensional observations of halo shapes are available.

Previous studies have found that the orientation of the major axis of a cluster is strongly affected by the direction of the most recently accreted subhalo, as seen

in simulations (van Haarlem & van de Weygaert 1993; Tormen 1997) and observations (Ebeling et al. 2004). If these are accreted from filaments, then there should be a strong alignment of cluster major axes with the filaments, as we have found. The minor axes are even more strongly aligned; this either suggests that recently accreted subhalos have a stronger effect on the minor axis than on the major axis, or more likely that figure rotation scrambles this alignment. Bailin & Steinmetz (2004) found that most halos (78%) show slow figure rotation about the minor axis, with a median pattern speed of  $\approx 0.15 h \text{ km s}^{-1} \text{ kpc}^{-1}$ , suggesting that the major axis of a typical halo can change by  $90^\circ$  in a Hubble time. However, only 13% of halos show figure rotation about their major axis. Therefore, even if a halo is formed with both its major and minor axes perfectly aligned with the filament, the major axis most often rotates away from that orientation by several degrees while the minor axis most often remains in its original orientation.

The galaxy mass halos show weaker alignment between their axes and the large scale structure than do the cluster mass halos. It may be that the axes of lower mass halos are less affected by recent major mergers, or that the direction of the accretion is more isotropic (Vitvitska et al. 2002). Aubert et al. (2004) find that the accretion onto halos at masses down to  $5 \times 10^{12} M_\odot$  is quite anisotropic; however, 97% of our “galaxy” mass halos lie below this limit. On the other hand, figure rotation may again be at work. Although Bailin & Steinmetz (2004) found no relationship between the figure rotation pattern speed and the halo mass, lower mass halos are on average dynamically older, and therefore figure rotation may have had a longer time to modify the original orientation. In any case, although we cannot directly test whether the correlation of the axes depends on mass, the strong dependence of axis alignment on mass suggests that the intrinsic alignments of galaxy mass halos are much weaker than the intrinsic alignments of cluster mass halos. Therefore, when interpreting weak lensing results, it is important to note that the predictions for the intrinsic alignments of galaxies made by analyzing cluster mass halos (e.g. Croft & Metzler 2000; Heavens et al. 2000) are likely overestimates.

Turning to the angular momentum, we find an intriguing correlation between the concentration of a halo  $c_{\text{vir}}$  and the tendency for its angular momentum to point toward other halos,  $\xi_{Lr}$  (see Figure 23). While most halos show no tendency for the angular momentum to point toward rather than away from nearby halos, halos with particularly high concentration parameters show positive  $\xi_{Lr}$ . The concentration parameter is a measure of the factor by which the halo has collapsed since its formation (Navarro et al. 1997); therefore non-linear effects and higher order terms in the expansion of the potential are expected to play a more important role in these halos. Indeed, in simple linear theory where the potential is approximated by a second-order Taylor expansion (White 1984), each axis is symmetric and so it is impossible to produce a preferred direction. However, a second-order expansion of the potential  $\Phi$  is only a solution to the Poisson equation in a constant density background. In order for the angular momentum to point toward nearby structure, there must be a background density gradient. In the simplest case, the potential must

be expanded to third order to account for a linear density gradient. Each additional derivative of the potential couples to additional moments of the density distribution of the protohalo (Porciani et al. 2002a). Therefore, the third derivatives of the potential couple to the skewness of the density distribution. Because the third derivatives are no longer symmetric (in general  $T_{ijj} \neq T_{ijj}$ , where  $T_{ijk} \equiv \partial^3 \Phi / \partial q_i \partial q_j \partial q_k$ ), the symmetry is broken and it is possible to produce a preferred direction.

The differences between the alignment of the angular momentum of low and high mass halos are also intriguing. Angular momentum is usually thought to either arise from the tidal torquing of an asymmetric protohalo (White 1984), or by the accretion of substructure on non-radial orbits (Tormen 1997; Vitvitska et al. 2002). In a sense, these are not distinct scenarios; accreted subhalos *are* protogalactic material that has been tidally torqued. However, the detailed orientation of the angular momentum may depend on the clumpiness of the accretion and other non-linear effects (Porciani et al. 2002a).

We find that the angular momentum in galaxy mass halos points parallel to the large scale structure, while the angular momentum in cluster mass halos points perpendicular to the large scale structure (see Figure 24). If the direction of the angular momentum is dominated by mergers of objects falling in along filaments, then the angular momentum will tend to point perpendicular to the velocity of the infalling objects, i.e. perpendicular to the filament. Therefore, the difference between the alignment of the angular momentum of the low and high mass halos suggests that the accretion onto low mass halos is either smoother than the accretion onto high mass halos, or that a significant fraction of the accretion in low mass halos occurs perpendicular to the filament (Vitvitska et al. 2002). The group and cluster mass halos, on the other hand, tend to occur at the intersections of large filaments, and have been built up by the recent accretion of halos along the filament which contribute angular momentum perpendicular to the filament (note that this confirms the suggestion of Maller et al. (2002) that accretion along a preferred axis is required to explain the distribution of spin parameters seen in simulated halos).

This difference between the inferred origin of the angular momentum of low and high mass halos meshes nicely with that of Peirani et al. (2004). These authors found that halos which have experienced a major merger acquired their angular momentum much more rapidly than those halos which grew only through steady accretion, suggesting that the sources of their angular momenta are the merger events. The halos in the merger sample also built up their mass more quickly due to those mergers, and consequently have larger median present-day masses. Our group and cluster mass halos thus contain a larger fraction of major merger products, and therefore a larger number of halos whose angular momenta were built up through mergers. It is encouraging that our results, based on the orientation of the angular momentum vectors, and the results of Peirani et al. (2004), which are based on the evolution of the magnitude of the angular momentum, build a consistent picture.

It is interesting to compare our results for collisionless dark matter halos with the results of Navarro et al.



(2004) for simulations that include baryonic physics. The main results of Navarro et al. (2004) are that the angular momenta of baryonic galactic disks in gasdynamical simulations tend to align with the intermediate axis of the local baryon distribution on scales of  $\approx 2 h^{-1}$  Mpc, and that observed edge-on disk galaxies in the local supercluster have their spin axes lying within the supergalactic plane, as expected in such a scenario. We find that on the scale of an individual halo, the angular momentum of the dark matter aligns with its minor axis. However, we also find that it lies parallel to the large scale structure, as expected if the spin vector lies within local sheet-like structures as suggested by Navarro et al. (2004). We also find that in low density regions, halo spins point toward nearby filaments, and are therefore aligned with the intermediate axis of the local density field. Therefore, despite the common presence of misalignments between the angular momenta of the baryons and the dark matter in individual galaxies (Sharma & Steinmetz 2004), each retains some memory of the initial torques provided by the large scale structure.

Unlike for galaxy mass halos, for which we can confirm that the angular momenta of the dark matter and baryons share similar relationships to the large scale structure in simulations, we do not have high resolution gasdynamical simulations of the more massive groups and clusters with which to compare. It may be possible to determine the rotation axis of baryons in these systems observationally. In theory, the spin vector of a relaxed cluster can be deduced from the presence of a redshift gradient of the galaxies in the cluster; however, confusion due to structure along the line of sight, the small magnitude of the rotation compared to the intrinsic velocity dispersion, ambiguity in the orientation of the ellipsoidal shape, intrinsic distance gradients, the lack of a large sample of substructureless relaxed clusters, and the uncertain relationship between the angular momentum of the cluster galaxies and that of the smooth X-ray emitting gas that dominates the baryonic mass make this measurement difficult. The rotation of the X-ray gas itself, however, may be measured using the kinematic Sunyaev-Zeldovich effect in future Cosmic Microwave Background (CMB) surveys (Chluba & Mannheim 2002; Cooray & Chen 2002).

## 7. SUMMARY

We have studied the internal shapes and angular momenta of galaxy and group mass dark matter halos formed in a  $\Lambda$ CDM  $N$ -body simulation, and studied how they are correlated with the large scale structure and the properties of neighbouring halos.

Internally, halos are triaxial with  $b/a$  and  $c/a$  ratios of  $0.75 \pm 0.15$  and  $0.6 \pm 0.1$  respectively. The distribution of axis ratios has a tail to low values. The two-dimensional projected ellipticities cover a broad range of values from 0 to 0.5, with a mean of 0.24, consistent with the weak lensing results of Hoekstra et al. (2004). The axis ratios rise between 0.12 and  $0.6 r_{\text{vir}}$ , beyond which they drop. Within  $0.12 r_{\text{vir}}$ , the measurement is probably compromised by the force softening in the simulations. Halos are most often prolate in the inner regions, but tend to a more even mix of prolate and oblate at large radii.

The internal alignment of the halos within  $0.6 r_{\text{vir}}$  is very good, particularly for the minor axis, with a slight

decrease in alignment in the outermost regions. High mass halos have particularly well-aligned axes. While the orientation of the angular momentum is also relatively constant, it changes more noticeably as a function of radius than do the axes; there is very little correlation between the very innermost regions and the very outermost regions. The distribution of spin parameters is essentially independent of the size of the region used to calculate it, indicating that the relative importance of the angular momentum is the same at all radii. At any given radius, the angular momentum vector tends to be aligned with the minor axis and be perpendicular to the major axis. However, the mean misalignment of  $\sim 25^\circ$  implies that galactic disks are generally misaligned with their halo. Figure rotation of the halo and reorientation of the disk due to newly accreted angular momentum act to maintain this misalignment. The alignment between the angular momentum and the principal axes gets weaker at larger radii. The properties of the halo at  $0.4 r_{\text{vir}}$  are quite characteristic of their values at most other radii.

The minor axes of halos show a strong tendency to lie perpendicular to the filaments. As a consequence, the major (and, to a lesser degree, intermediate) axes tend to point along filaments. Figure rotation about the minor axis may be responsible for the smaller degree of major axis alignment. These alignments fall off with distance as a power law. In all cases, the alignment for group and cluster mass halos is stronger and extends to much larger separations than for galaxy mass halos. Therefore, previous studies which predict the intrinsic alignments of galaxies based on the shapes of cluster mass halos appear to systematically overestimate the correlations. The major axes of halos show a weak correlation with those of other nearby halos, while there is no robust detection of a correlation for the intermediate or minor axes.

The angular momenta of high-concentration halos tend to point toward, rather than away from, nearby halos. These halos have collapsed further into the non-linear regime, and therefore the effects of higher-order derivatives of the tidal field, which are necessary to create a preferential direction, are more important for these halos. The angular momenta of halos in low density environments also tend to point toward local density enhancements, in agreement with the results of Kashikawa & Okamura (1992) for galaxies  $2 h^{-1}$  Mpc or more away from the local supergalactic plane. The angular momenta of galaxy mass halos show a weak tendency to point along filaments on scales up to  $3 h^{-1}$  Mpc, but those of group and cluster mass halos show a very strong tendency to point perpendicular to the filaments. This appears to be due to the different merger histories of the two samples; higher mass halos are more likely to have experienced a major merger along a filament which dominated the evolution of their angular momentum, while lower mass halos are more likely to have had a smoother accretion history. We detect no correlations between the angular momentum directions of nearby halos, but due to the size of the error bars, this is consistent with previous linear and  $N$ -body studies that predict weak correlations. Comparisons with recent gasdynamical simulations and observations of edge-on disk galaxies in the local supercluster suggest that both the baryons and dark matter in galaxies share a memory of the orientation of

the large scale structure that provided the initial torque. The alignments we predict may be tested with large samples of galaxy redshifts within relaxed clusters, or by kinematic Sunyaev-Zeldovich studies in future CMB experiments.

This work has been supported by grants from the U.S.

National Aeronautics and Space Administration (NAG 5-10827), the David and Lucile Packard Foundation, the Bundesministerium für Bildung und Forschung (FKZ 05EA2BA1/8), and by the American Astronomical Society and the National Science Foundation in the form of an International Travel Grant.

#### REFERENCES

- Argyres, P. C., Groth, E. J., Peebles, P. J. E., & Struble, M. F. 1986, *AJ*, 91, 471
- Aubert, D., Pichon, C., & Colombi, S. 2004, *MNRAS*, 352, 376
- Bailin, J. 2004, PhD thesis, University of Arizona
- Bailin, J., & Steinmetz, M. 2004, *ApJ*, 616, 27
- Barnes, J., & Efstathiou, G. 1987, *ApJ*, 319, 575
- Binggeli, B. 1982, *A&A*, 107, 338
- Binney, J., Jiang, I., & Dutta, S. 1998, *MNRAS*, 297, 1237
- Brown, M. L., Taylor, A. N., Hambly, N. C., & Dye, S. 2002, *MNRAS*, 333, 501
- Bullock, J. S. 2002, in “The shapes of galaxies and their dark halos”, Proceedings of the Yale Cosmology Workshop, New Haven, Connecticut, USA, 28-30 May 2001., ed. Priyamvada Natarajan (Singapore: World Scientific), 109
- Bullock, J. S., Dekel, A., Kolatt, T. S., Kravtsov, A. V., Klypin, A. A., Porciani, C., & Primack, J. R. 2001a, *ApJ*, 555, 240
- Bullock, J. S., Kolatt, T. S., Sigad, Y., Somerville, R. S., Kravtsov, A. V., Klypin, A. A., Primack, J. R., & Dekel, A. 2001b, *MNRAS*, 321, 559
- Buote, D. A., Jeltema, T. E., Canizares, C. R., & Garmire, G. P. 2002, *ApJ*, 577, 183
- Cabanela, J. E., & Dickey, J. M. 1999, *AJ*, 118, 46
- Chambers, S. W., Melott, A. L., & Miller, C. J. 2002, *ApJ*, 565, 849
- Chluba, J., & Mannheim, K. 2002, *A&A*, 396, 419
- Colberg, J. M., White, S. D. M., Jenkins, A., & Pearce, F. R. 1999, *MNRAS*, 308, 593
- Cole, S., & Lacey, C. 1996, *MNRAS*, 281, 716
- Cooray, A., & Chen, X. 2002, *ApJ*, 573, 43
- Crittenden, R. G., Natarajan, P., Pen, U., & Theuns, T. 2001, *ApJ*, 559, 552
- Croft, R. A. C., & Metzler, C. A. 2000, *ApJ*, 545, 561
- Debattista, V. P., & Sellwood, J. A. 1999, *ApJ*, 513, L107
- Dekel, A., & Shlosman, I. 1983, in *IAU Symp. 100: Internal Kinematics and Dynamics of Galaxies*, 187
- Doroshkevich, A. G. 1970, *Astrofizika*, 6, 581
- Dubinski, J. 1992, *ApJ*, 401, 441
- . 1994, *ApJ*, 431, 617
- Dubinski, J., & Carlberg, R. G. 1991, *ApJ*, 378, 496
- Ebeling, H., Barrett, E., & Donovan, D. 2004, *ApJ*, 609, L49
- Faltenbacher, A., Gottlöber, S., Kerscher, M., & Müller, V. 2002, *A&A*, 395, 1
- Flin, P. 1987, *MNRAS*, 228, 941
- Franx, M., Illingworth, G., & de Zeeuw, T. 1991, *ApJ*, 383, 112
- Frenk, C. S., White, S. D. M., Davis, M., & Efstathiou, G. 1988, *ApJ*, 327, 507
- Gerhard, O. E. 1983, *MNRAS*, 202, 1159
- Han, C., Gould, A., & Sackett, P. D. 1995, *ApJ*, 445, 46
- Hatton, S., & Ninin, S. 2001, *MNRAS*, 322, 576
- Heavens, A., Refregier, A., & Heymans, C. 2000, *MNRAS*, 319, 649
- Helmi, A. 2004a, *MNRAS*, 351, 643
- . 2004b, *ApJ*, 610, L97
- Heyl, J. S., Hernquist, L., & Spergel, D. N. 1994, *ApJ*, 427, 165
- Hoekstra, H., Yee, H. K. C., & Gladders, M. D. 2004, *ApJ*, 606, 67
- Holmberg, E. 1974, *Arkiv for Astronomi*, 5, 305
- Hopkins, P. F., Bahcall, N. A., & Bode, P. 2005, *ApJ*, 618, 1
- Ibata, R., Lewis, G. F., Irwin, M., Totten, E., & Quinn, T. 2001, *ApJ*, 551, 294
- Jenkins, A., Frenk, C. S., Pearce, F. R., Thomas, P. A., Colberg, J. M., White, S. D. M., Couchman, H. M. P., Peacock, J. A., Efstathiou, G., & Nelson, A. H. 1998, *ApJ*, 499, 20
- Jing, Y. P., & Suto, Y. 2000, *ApJ*, 529, L69
- . 2002, *ApJ*, 574, 538
- Johnston, K. V., Law, D. R., & Majewski, S. R. 2005, *ApJ*, 619, 800
- Kashikawa, N., & Okamura, S. 1992, *PASJ*, 44, 493
- Kasun, S. F., & Evrard, A. E. 2004, *ApJ*, submitted, (astro-ph/0408056) (KE04)
- Kazantzidis, S., Kravtsov, A. V., Zentner, A. R., Allgood, B., Nagai, D., & Moore, B. 2004, *ApJ*, 611, L73
- Knebe, A., Gill, S. P. D., Gibson, B. K., Lewis, G. F., Ibata, R. A., & Dopita, M. A. 2004, *ApJ*, 603, 7
- López-Corredoira, M., Betancort-Rijo, J., & Beckman, J. E. 2002, *A&A*, 386, 169
- Lambas, D. G., Groth, E. J., & Peebles, P. J. E. 1988, *AJ*, 95, 996
- Lambas, D. G., Nicotra, M., Muriel, H., & Ruiz, L. 1990, *AJ*, 100, 1006
- Law, D. R., Johnston, K. V., & Majewski, S. R. 2005, *ApJ*, 619, 807
- Lee, J., & Pen, U. 2000, *ApJ*, 532, L5
- . 2001, *ApJ*, 555, 106
- Lee, J., & Suto, Y. 2003, *ApJ*, 585, 151
- . 2004, *ApJ*, 601, 599
- Maller, A. H., Dekel, A., & Somerville, R. 2002, *MNRAS*, 329, 423
- Martínez-Delgado, D., Gómez-Flechoso, M. Á., Aparicio, A., & Carrera, R. 2004, *ApJ*, 601, 242
- Muriel, H., & Lambas, D. G. 1989, *AJ*, 98, 1995
- Natarajan, P., & Refregier, A. 2000, *ApJ*, 538, L113
- Navarro, J. F., Abadi, M. G., & Steinmetz, M. 2004, *ApJ*, 613, L41
- Navarro, J. F., Frenk, C. S., & White, S. D. M. 1996, *ApJ*, 462, 563
- . 1997, *ApJ*, 490, 493
- Olling, R. P., & Merrifield, M. R. 2000, *MNRAS*, 311, 361
- Onuora, L. I., & Thomas, P. A. 2000, *MNRAS*, 319, 614
- Ostriker, E. C., & Binney, J. J. 1989, *MNRAS*, 237, 785
- Peebles, P. J. E. 1969, *ApJ*, 155, 393
- Peirani, S., Mohayaee, R., & de Freitas Pacheco, J. A. 2004, *MNRAS*, 348, 921
- Pen, U., Lee, J., & Seljak, U. 2000, *ApJ*, 543, L107
- Plionis, M. 1994, *ApJS*, 95, 401
- Porciani, C., Dekel, A., & Hoffman, Y. 2002a, *MNRAS*, 332, 325
- . 2002b, *MNRAS*, 332, 339
- Quinn, T., & Binney, J. 1992, *MNRAS*, 255, 729
- Rhee, G. F. R. N., & Katgert, P. 1987, *A&A*, 183, 217
- Sackett, P. D. 1999, in *ASP Conf. Ser. 182: Galaxy Dynamics - A Rutgers Symposium*, ed. D. Merritt, J. A. Sellwood, & M. Valluri, 393
- Sackett, P. D., Rix, H., Jarvis, B. J., & Freeman, K. C. 1994, *ApJ*, 436, 629
- Sarazin, C. L. 1986, *Rev. Mod. Phys.*, 58, 1
- Sharma, S., & Steinmetz, M. 2004, *ApJ*, submitted, (astro-ph/0406533)
- Splinter, R. J., Melott, A. L., Linn, A. M., Buck, C., & Tinker, J. 1997, *ApJ*, 479, 632
- Stark, A. A. 1977, *ApJ*, 213, 368
- Struble, M. F., & Peebles, P. J. E. 1985, *AJ*, 90, 582
- Sugerman, B., Summers, F. J., & Kamionkowski, M. 2000, *MNRAS*, 311, 762
- Sunyaev, R. A., & Zeldovich, I. B. 1980, *ARA&A*, 18, 537
- Toomre, A. 1983, in *IAU Symp. 100: Internal Kinematics and Dynamics of Galaxies*, 177
- Tormen, G. 1997, *MNRAS*, 290, 411
- Ulmer, M. P., McMillan, S. L. W., & Kowalski, M. P. 1989, *ApJ*, 338, 711
- Černe, J., & Peterson, J. B. 1990, *AJ*, 100, 1761
- van den Bosch, F. C., Abel, T., Croft, R. A. C., Hernquist, L., & White, S. D. M. 2002, *ApJ*, 576, 21
- van Haarlem, M., & van de Weygaert, R. 1993, *ApJ*, 418, 544
- Vitvitska, M., Klypin, A. A., Kravtsov, A. V., Wechsler, R. H., Primack, J. R., & Bullock, J. S. 2002, *ApJ*, 581, 799
- Warren, M. S., Quinn, P. J., Salmon, J. K., & Zurek, W. H. 1992, *ApJ*, 399, 405

- West, M. J., Jones, C., & Forman, W. 1995, ApJ, 451, L5
- West, M. J., Villumsen, J. V., & Dekel, A. 1991, ApJ, 369, 287
- White, S. D. M. 1984, ApJ, 286, 38
- Zaritsky, D., Smith, R., Frenk, C. S., & White, S. D. M. 1997, ApJ, 478, L53
- Zibetti, S., White, S. D. M., & Brinkmann, J. 2004, MNRAS, 347, 556